Electronic Raman scattering on the $Ba(Fe_{1-x}Co_x)_2As_2$ ferropnictide unconventional superconductor for determination of the superconducting gap symmetry

Bachelor Thesis by:

Rolf B. Versteeg
Optical Condensed Matter Physics
University of Groningen

university of groningen / faculty of mathematics and natural sciences

1st supervisor:	Prof. Dr. Ir. P.H.M. van Loosdrecht
2nd supervisor:	A. Caretta
Period:	April 2011 – July 2011

Electronic Raman scattering on the $Ba(Fe_{1-x}Co_x)_2As_2$ ferropnictide unconventional superconductor for determination of the superconducting gap symmetry

Bachelor Thesis by:

Rolf B. Versteeg
Optical Condensed Matter Physics
University of Groningen

Contents

1 Motivation

In advance of writing I made some considerations on what to include and how to write this thesis regarding “language”. The three key elements of the title are “electronic Raman Scattering”,“ferropnictide” and “gap symmetry”. All these topics have lengthy review articles with a lot of interesting points, but those writers treat these points way better that I can do, so my goal was to make a “best of” unification especially geared towards these three key elements. Over the past few months there were of course struggles with understanding the articles published on *Raman Scattering on iron pnictides for determination of the gap symmetry.* The theoretical part of this thesis was written with the idea that a layman (say “peers”) on this topic is capable of following articles by for instance *Muschler et al.* and *Sugai et al.* in detail after reading this chapter. Hopefully this “review” part will circumvent the struggles I had for future students on this topic.

Furthermore, I have written the thesis with the idea that it should be readable to peers. This means that a 3th year physics student should be able to follow the text provided they have indeed taken a course in Solid State Physics and have familiarized themselves with concepts as the Brillouin Zone, Fermi surfaces, phonons, band theory, etcetera. This also means that I did not include a part on the classical treatment of superconductivity. For this I would refer to Kittel’s Solid State Physics book.

There is a danger in describing “peers”. Not every 3th year physics student took a course on symmetry principles in Physics (group theory and selection rules). It would be tedious to address this topic to its full extent in a bachelor thesis. It merely serves as an “aid” in this research field and it is not the main topic of my bachelor project, so I skipped the discussion of this topic. So this is where I make a dangerous assumption. If one wants to read about symmetry principles and its applications in Raman spectroscopy I would refer to the following books:

- *Groups, representations and physics* by H.F. Jones for a good description on discrete groups.
- *Solid-State Spectroscopy* by H. Kuzmany for the applications of group theory to selection rules.

Chapter 2 of this thesis consists of a description of ferropnictide superconductors and gap symmetries. In chapter 3 electronic Raman scattering will be addressed and its benefits for determination of superconducting gaps. A great deal of attention to the theoretical discussion is paid as it is nontrivial . Chapter 4 goes through the used experimental setups and the properties of the studied sample are considered.

Chapter 5 consists of results and a discussion of the results. The initial aim was to acquire data to determine superconducting gap symmetries in $Ba(Fe_{1-x}Co_x)_2As_2$, but the used setup showed not to be appropriate for this goal as will be discussed. Also the phonons in the studied material will be discussed as they posed serious questions during the project.

2 Theoretical consideration on the material

2.1 The iron-based superconductors: an overview

The research field of iron pnictide superconductors started in 2008 with the discovery of superconducting transition temperatures up to T_c=28K in $LaFeAsO_{1-x}F_x$ with x=0.11 by Hideo Hosono and co-workers. [1] In the past the antagonistic relationship between superconductivity and magnetism has led researchers to avoid (ferro)magnetic elements as building blocks for new superconductors. [2] The presence of these elements makes, apart from a superconducting state in the material, also an antiferromagnetic phase possible.

The superconducting phase is induced upon doping of the parent compound. Apart from the SC-phase, other exotic phases in the pnictides can be reached by specific doping parameters.

For the $Ba(Fe_{1-x}Co_x)_2As_2$ materials the phase diagram is given in Figure 2-1. There is an antiferromagnetic region (AFM) in light blue and a green region where AFM and superconductivity coexist. The superconducting phase is reached by a doping parameter between x≈0,03 and x≈0,12 The material studied has a doping parameter x≈0,10 which gives a T_c≈22K.

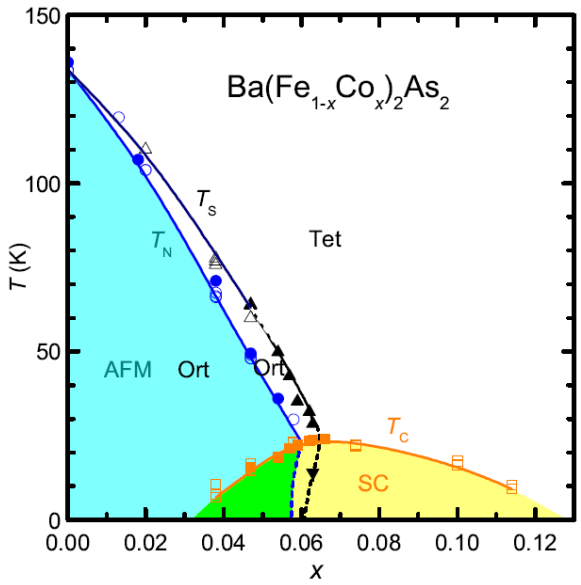

Figure 2-1. Phase diagram $Ba(Fe_{1-x}Co_x)_2As_2$

2.2 Classes

Up to date, 6 different structural classes of ferropnictide superconductors have been found .[3,4] They can be classified according to the stochiometric coeffients of their mother compound (non-doped material):

- 11: e.g. the $Fe_{1+y}(Se_xTe_{1-x})$-system
- 111: e.g. LiFeAs
- 1111: e.g. LaFeAsO
- 122: e.g. $Ba(Fe_{1-x}Co_x)_2As_2$
- A more complicated 1111-type with a perovskite-like interlayer, e.g. $Sr_3Sc_2O_5Fe_2As_2$
- 235: a new class with 5 thick perovskite-like interlayers between the iron-arsenide planes.

The main ingredient to all of these classes is a quasi-2D-layer consisting of a square lattice of iron atoms joined by tetrahedrally coordinated atoms from the 15th and 16th column of the periodic table;

[1] (Johnston, 2010, page 806)
[2] (Paglione & Greene, 2010, page 645)
[3] (Paglione & Greene, 2010, page 647)
[4] (Ogino, March 21-25, 2011)

the pnictogen group (P,As) and chalcogen group (S,Se,Te) respectively. As the pnictogen and chalcogen anions are staggered above and below the iron lattice, the unit cell of this layer is doubled. These layers can be stacked together as in the $Fe_{1+y}(Se_xTe_{1-x})$-system (11-compound) to give the simplest form of a ferropnictide SC. There is also the possibility of blocking layers between the iron-arsenide planes. This provides a quasi-2D-character to the crystal because of the ionic character of the bonds between the layers. The blocking-layers can consist of for instance a alkaline-earth layer (Ba) to give rise to the 122 $Ba(Fe_{1-x}Co_x)_2As_2$ pnictide. Figure 2-2 gives an overview of the 5 different tetragonal structures. [1] The studied sample $Ba(Fe_{1-x}Co_x)_2As_2$ has the same unit cell as the $BaFe_2As_2$ unit cell portrayed below except for cobalt substitutions. The blue atoms are barium, the red atoms iron/cobalt and the arsenide atoms are yellow.

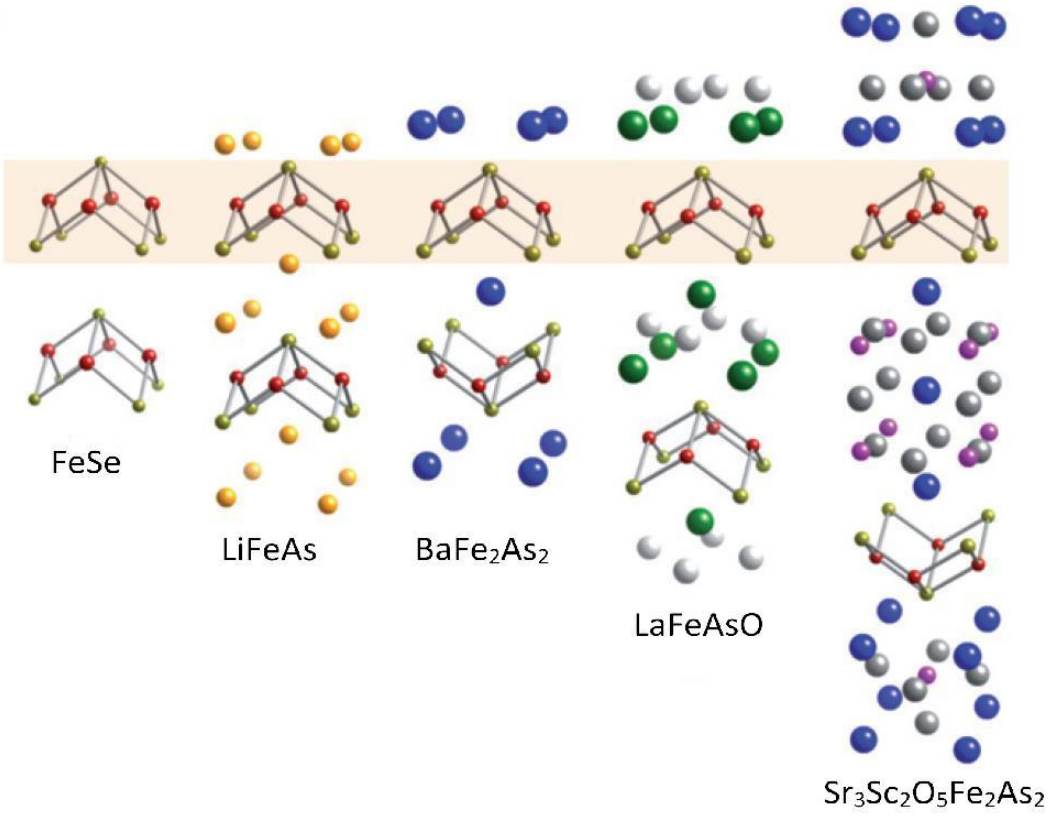

Figure 2-2. The first 5 families of ferropnictide superconductors.[2]

The 11,111,111-compounds are primitive tetragonal structures above T_c, which is the P4/nmm space group or no. 129 space group. The 122-type belongs to the body-centered-tetragonal space group, which is the P4/mmm group or no. 139 group. Below a material specific temperature T_0 a first-order structural phase transition to Fmmm orthorhombic bcc can arise for the 122 class. [3]

[1] (Johnston, 2010), Introduction and overview

[2] (Paglione & Greene, 2010)

[3] (Johnston, 2010), page 820

2.3 Brillouin Zones

The Brillouin Zones of the 122-type materials distinguishes from the Brillouin Zones of the 11,111,1111-compounds, as they do not belong to the same symmetry group.[1]

2.3.1 11,111,1111-compounds

The reciprocal lattice of the primitive tetragonal real lattice (11,111,1111-compound) is another primitive tetragonal lattice. The $\mathbf{k}_x$, $\mathbf{k}_y$ and $\mathbf{k}_z$ axes of the Brillouin Zone are given as follows:

$$\boldsymbol{k}_x = \frac{2\pi}{a}(\boldsymbol{a}) \qquad \boldsymbol{k}_y = \frac{2\pi}{a}(\boldsymbol{b}) \qquad \boldsymbol{k}_z = \frac{2\pi}{a}(\boldsymbol{c}) \tag{2.3.1}$$

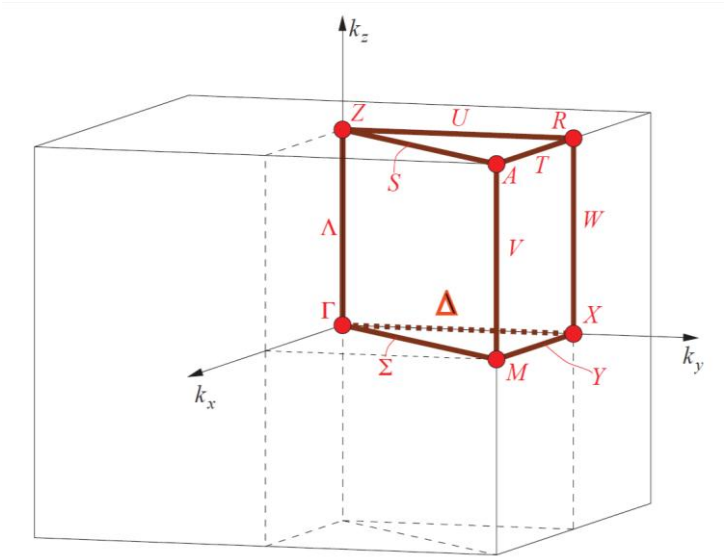

Figure 2-3 Brillouin Zone of 11,111,1111-compounds[2]

Figure 2-3 depicts the Brillouin Zone of the no.129 space group. In articles in the ferropnictide research field one mostly find only the $\mathbf{k}_x$, $\mathbf{k}_y$-plane portrayed as this is where the electronic structure of the material is situated in the Brillouin Zone.

2.3.2 122-compounds

The Brillouin Zone of the 122-compounds is somewhat more difficult. The reciprocal lattice of the body centered tetragonal (bct) real-space lattice is another bct lattice as in Figure 2-4:

[1] (Johnston, 2010, page 826-834)

[2] (Johnston, 2010)

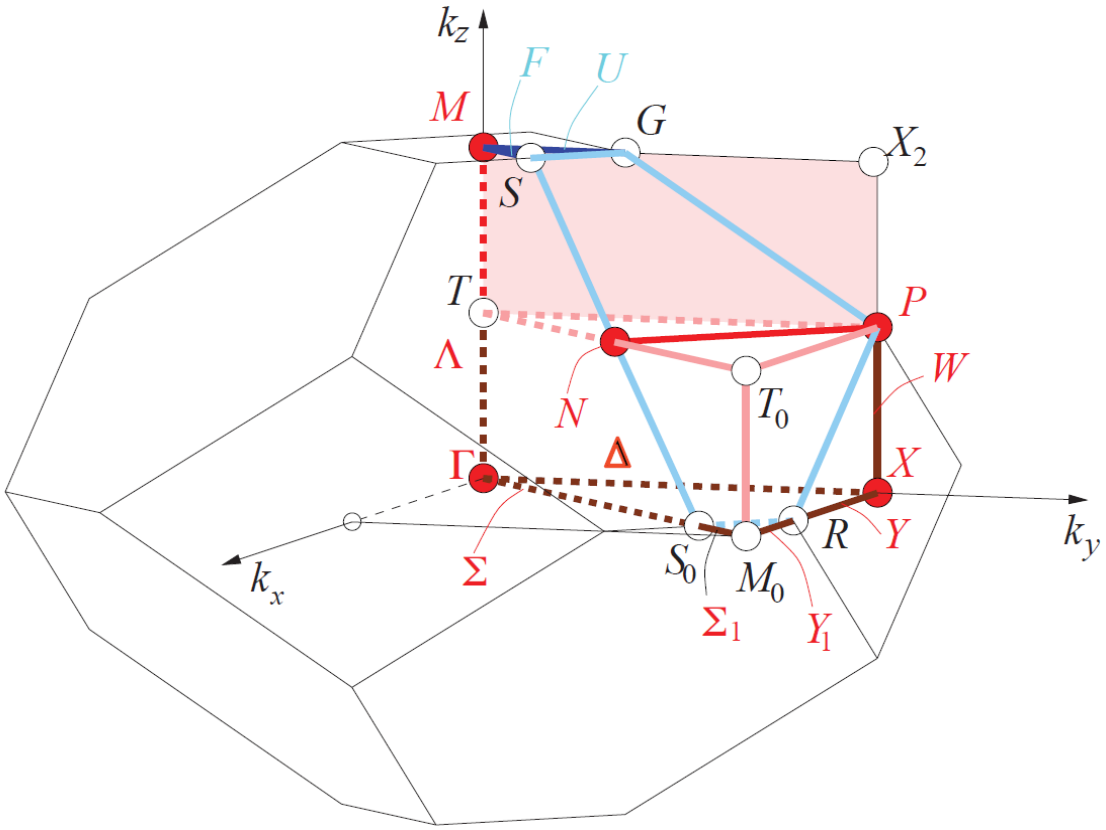

Figure 2-4. BZ for body-centered-tetragonal space group I4/mmm (No.139) [1]

There are some important remarks to be made on the Brillouin zone of the bct. In articles in the iron-pnictide research field this Brillouin Zone is mostly pictured in a more simple way as a rectangular parallelopiped or it's ($\mathbf{k}_x$,$\mathbf{k}_y$)-plane projection with the M-points in the corner and X-points in the centre of an edge.

Furthermore, the reciprocal lattice axes $\mathbf{k}_x$ and $\mathbf{k}_y$ are 45° rotated with respect to the **a** and **b** axes of the direct lattice. This gives as an expression for the bct Brillouin Zone with direct lattice constants *a*,*b* and *c*:

$$\boldsymbol{k}_x = \frac{2\pi}{a}(\boldsymbol{a}-\boldsymbol{b}) \qquad \boldsymbol{k}_y = \frac{2\pi}{a}(\boldsymbol{a}+\boldsymbol{b}) \qquad k_z = \frac{4\pi}{a}(\boldsymbol{c}) \tag{2.3.2}$$

This 45° rotation makes that some attention needs to be paid in literature to which point of the Brillouin Zone is meant.

Finally, there is one remark to be made on the terms "folded Brillouin Zone" and "unfolded Brillouin Zone" to which researchers frequently refer in their articles. Irrespective of to which class a certain ferropnictide belongs (11,111,1111,122-class), the FeAs-layer has two Fe atoms (Fe_2) per unit cell. The *folded BZ* of the FeAs-layer direct lattice refers to the BZ of the actual crystal structure where there are two Fe atoms and two As atoms per FeAs-layer. The *unfolded BZ* refers to the use of a

[1] (Johnston, 2010)

primitive tetragonal as a direct lattice with only one Fe atom in each layer where the presence of pnictogens or chalchogens are ignored. [1]

2.4 Electronic structure of the FeAs-layer

The FeAs-layer is held together by a combination of covalent bonds (Fe-As-bonding) and metallic bonds (Fe-Fe-bonding). The d-orbitals of the Fe^{2+}(…$3d^6$) anion are fivefold degenerate. This Fe^{2+} anion is surrounded by four As^{3-} cations coordinated in a tetrahedron. By the inclusion of a crystal field by the arsenides the fully rotational site symmetry of Fe^{2+} is broken. The Fe^{2+} five d-orbital degeneracy is lifted by this symmetry breaking. The energy levels split into a low energy set of two e_g orbitals $d_{x^2-y^2}$ and d_{z^2} and a more energetic threefold degenerate t_{2g} state consisting of the original d_{xy}, d_{xz} and d_{yz} levels. The t_{2g} state is more energetically as the $d_{x^2-y^2}$ and d_{z^2} orbitals are oriented towards the arsenide cations. In the copper oxide superconductors this splitting can be clearly seen. However, the five d-orbitals in the iron arsenide materials show to be about the same energy. Hence, the bands formed by the d-orbitals in $Ba(Fe_{1-x}Co_x)_2As_2$ overlap to a large extent near the Fermi energy. In the Brillouin Zone this shows up as two closely positioned bands around high symmetry points as in Figure 2-7.

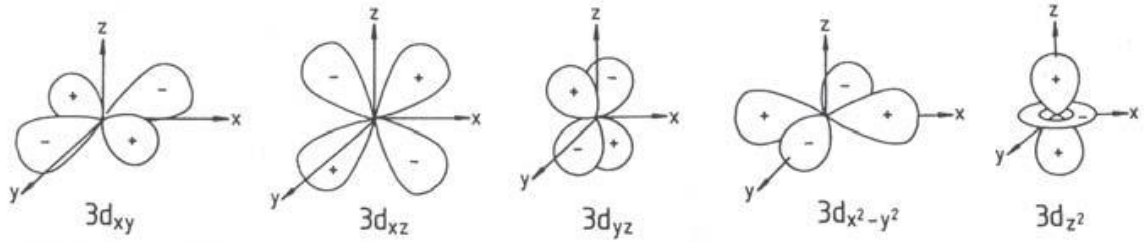

Figure 2-5 The five different d-orbitals for the Fe^{2+} anion.

The arsenide 4p orbitals do not account much to the density of states. This indicates that the conduction of the ferropnictides in the normal metallic phase is due to hopping of electrons from Fe atom to Fe atom instead of Fe atom to As atom to Fe atom. This is a big difference to the high T_c cuprates where conduction carriers hop from Cu to O to Cu in the CuO-plane. [2]

[1] (Johnston, 2010), page 835

[2] (Johnston, 2010), page 824

An important chararacteristic of the ferropnictides is that they are *semimetals* in their normal state. This means that the valence and conduction band of the material have an overlap in energy and by this electrons from the valence band can spill over to the conduction band. So there will even be conductivity at T=0. “holes” will give rise to conductivity in the top of the valence band at the Fermi level and “electrons” will give rise to conductivity in the bottom at the Fermi level of the conduction band. This will give rise to electron and hole “pockets” which allows for a new type of electron pairing, the so-called $s^{\pm}$-pairing. [1] This semimetal specific type of pairing has an opposite sign for the superconducting gap function for the electron and hole band respectively as will be discussed later. (Superconducting properties)

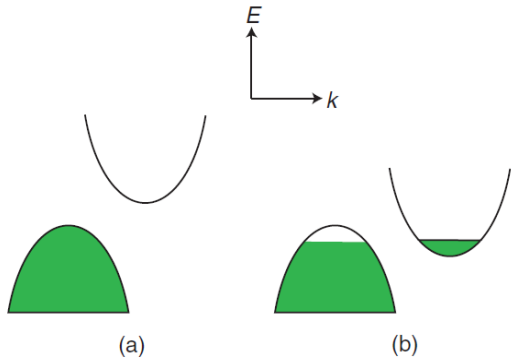

Figure 2-6. Pictorial view of band diagram of (a) indirect band gap semiconductor at T=0 with a filled valence band and an empty conduction band. At T=0 the material is an insulator. (b) semimetal. Even at T=0 there is conductivity. The current carriers in the valence band are “holes” and the current carriers in the conduction band are “electrons”. (Johnston)

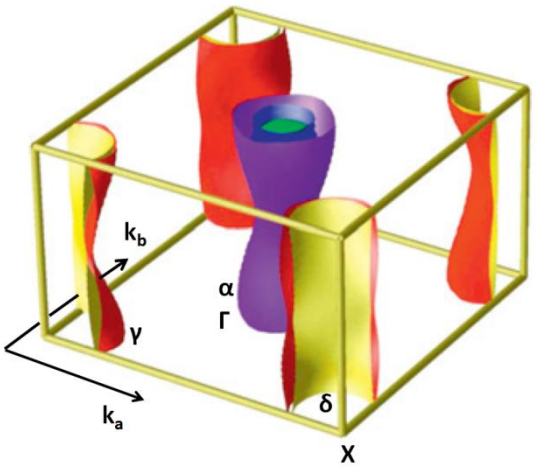

Figure 2-7. Fermi Surface of $Ba(Fe_{0,9}Co_{0,1})_2As_2$ as calculated by DFT. At the Γ-point the α-bands or hole bands are shown. The X-points show the δ–bands or electron bands. (Paglione)

Figure 2-6 is just a pictorial cut-through of the (E,**k**)-dispersion in one direction of the Brillouin Zone. Nonetheless, the argument of hole and electron pockets also works for a Brillouin Zone in both $\mathbf{k}_x$ and $\mathbf{k}_y$ direction. The band structure ($E(\mathbf{k}_x,\mathbf{k}_y)$) is a 3D plot which can be calculated by density functional theory . This band structure was already calculated for the material studied for this thesis: $Ba(Fe_{0,9}Co_{0,1})_2As_2$ (given in Figure 2-7) . It has hole-like Fermi-Surface-pockets at the Γ-point (the α-bands) and M-point (β-bands) of the Brillouin Zone and electron pockets at the X-points (γ-bands and δ-bands) (Figure 2-8)[2]. There are two bands around a high symmetry point due to the splitting of the five degenerate d-orbitals as discussed above.

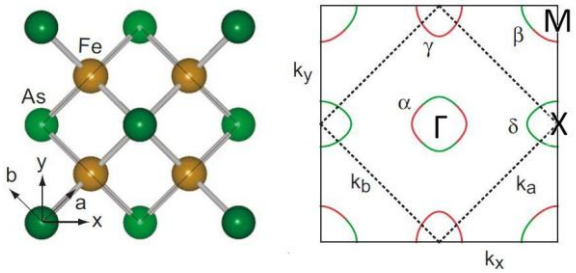

Figure 2-8 FeAs-plane and its Brillouin Zone with the relevant nomenclature as used in literature.

In Figure 2-8 the FeAs-plane is shown[3]. The Fe-As-Fe-bonds are in the direction of the **ab**-axes so this picture is rotated 45° with respect to the unit cell in Figure 2-2. The Brillouin Zone axes are again rotated over 45° with respect to the crystal axes **a** and **b** according to equations 3.3.2.

[1] (Johnston, 2010), page 825-826

[2] (Paglione & Greene, 2010), page 649

[3] Picture taken from (S.Sugai, 2010)

2.5 Superconducting properties

The superconducting state consists of electron pairs named Cooper pairs. The electrons forming a Cooper pair are located on positions **+k** and **-k** in the Brillouin Zone at the Fermi level around a band. As electrons are fermions with a spin s=1/2, the sign of the wave function of a Cooper pair must change under interchange of the electrons. Almost all known superconductors pair up with spins opposite to each other to give a singlet superconductor. With the spins anti-parallel, the orbital quantum number l of a Cooper pair (with momentum $L = \hbar\sqrt{l(l+1)}$) must be an integer to fulfill the Pauli principle, so l must be zero or an even integer. If $l = 0$ this will give an s-wave and if $l = 2$ this will give a d-wave for instance. For completeness; electrons paired up with spins in same direction will give rise to a "p-wave/f-wave superconductor". [1] By Knight-shift measurements a direct indication of the net spin of a Cooper pair can be measured (Knight Shift $K \sim \langle S_z \rangle$). [2]. For $Ba(Fe_{0.9}C_{0,1})_2As_2$ a S=0 was found to leave s-wave and d-wave as possible symmetries for this compound. [3]

Although the exact nature of the pairing mechanism for ferropnictides is not known at present a lot of research has already been done to determine the pairing symmetry. Conventional superconductors have a constant gap function Δ(**k**) around a Fermi surface, the *s-wave*. The gap function Δ(**k**) or superconducting order parameter is a complex function with both an amplitude and phase that describes the macroscopic quantum state of a Cooper pair. The gap function can also be expressed as Δ(θ). Here θ refers to the angle which the position of one electron of the Cooper pair makes with respect to the k_x-axis of the Brillouin Zone (two-particle picture). The length at the specific θ of the pictured lobe gives the gap energy. For an s-wave, all the Cooper pairs have the same gap energy. The Fermi Surface is fully gapped in the superconducting state as in Figure 2-9a. Another possibility is to have an *anisotropic s-wave superconductor* where Δ(θ) has a fluctuating amplitude but remains having a positive sign along the Fermi Surface as in Figure 2-9b. When $\Delta_{min}=0$ the gap becomes 0 but *does not go through zero*. This is sometimes referred to as the "kissing-mode" where the Fermi surface is just "kissed" by the gap function. For cuprate high-T_c's a singlet d-wave symmetry is favored. A d-wave symmetry has a gap function Δ(θ) which changes its sign along a Fermi Surface and accordingly has a nodal point situated at the Fermi energy (not fully gapped) as in Figure 2-9c. For instance, the electrons forming a Cooper pair situated on $\mathbf{k_x} = \mathbf{k_y}$ make a θ=45° with the k_x-axis. This gives a zero gap energy. The two electrons situated at $+\mathbf{k_x}$ and $-\mathbf{k_x}$ at the Fermi level make a Cooper pair with $+\Delta_0$.

[1] (Johnston, 2010), page 954

[2] (Kittel, 2005), page 378

[3] (Johnston, 2010), page 954

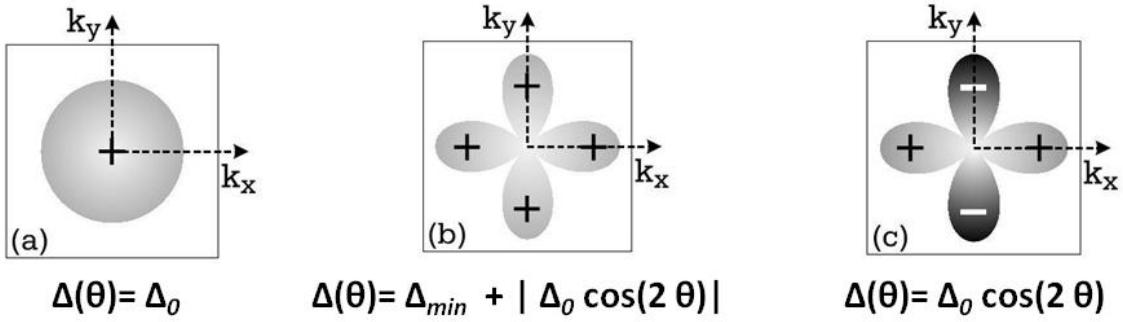

Figure 2-9 (a) s-wave (b) anisotropic s-wave (θ is the angle in k-space) (c) d-wave [1]

In ferropnictides a new s-wave-type symmetry is possible due to the existence of different bands in the electronic structure; the so-called $s^{\pm}$-wave-symmetry. [2] Here the sign of the gap function differs between the hole band (plus sign) and the electron band (minus sign) but the amplitude of Δ(θ) remains constant over a band (see Figure 2-10). If one is still not convinced of the richness in gap symmetry varieties then another function can be the combination of "anisotropic s-wave" and "$s^{\pm}$-wave" to give the anisotropic $s^{\pm}$-wave or *extended s*-wave. [3] Determining a sign, hence determining phase, is a difficult task as most experiments can only probe amplitude (Josephson-junctions can probe phase differences). So determining the difference between s-wave and $s^{\pm}$-wave can be quite complicated. In the next chapter a discussion will follow about how Raman-spectroscopy serves as a good probe to determine different wave-symmetries.

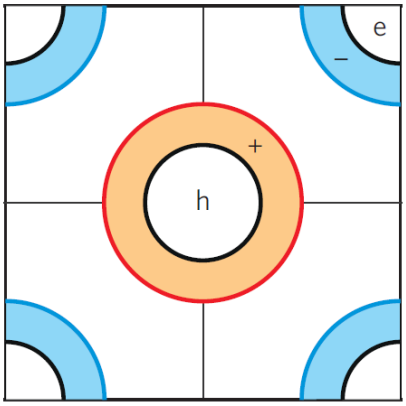

Figure 2-10 $s^{\pm}$-wave [4]

[1] Figure adapted from (Muschler B. , 2007)

[2] (Paglione & Greene, 2010), page 649

[3] (Boyd & Devereaux, Effect of disorder on the electronic Raman scattering in the superconducting state of iron pnictides, 2010)

[4] Figure adapted from (Paglione & Greene, 2010)

3 Electronic Raman scattering

3.1 Introduction

Raman scattering is a photon-in photon-out process with energy transferred to a target material. Most of the photons are elastically scattered. Some of the incoming photons absorb the energy and momentum (with momentum transfer $\Delta\mathbf{p}\approx 0$) of an elementary excitation in a material (anti-Stokes-scattering). This shift in energy can be measured. Another possibility is that the energy of an incoming photon is split to create an elementary excitation in the material and a photon with a lower energy (Stokes-scattering). Apart from a coupling to familiar excitations as phonons and magnons there is also the possibility that light couples to electronic charge in solids. This will give a variation of electronic charge density in the material. The measured frequency shift and polarization state of outcoming photons give information about the properties of charge-density relaxations in the material. Symmetry elements of a material can be linked to experimental polarization geometries as will be discussed in this chapter. This makes Raman Spectroscopy a technique which can focus on electron dynamics in different parts of the Brillouin Zone just by choosing the appropriate polarization components. [1]

A description of Raman scattering always starts with a description applicable to molecules where after this description is generalized to crystals. [2] A few words will be spent on this elementary description and then I will go on to describe the electronic Raman scattering, especially as a probe for determination of the gap function symmetry in superconductors.

3.2 Classical description

The Raman effect originates from a change in the polarizability of molecules (or the susceptibility of crystals) by the excited quasi-particles. A two-atom molecule with polarizability α_0 in the presence of a periodic electromagnetic field $E(\omega) = E_0\cos(\omega t)$ will give a time-dependent dipole moment $P_D(\omega) = \alpha_0 E(\omega)$.

If the molecule is vibrating with frequency Ω the distance between both atoms will be modulated. In this case the total dipole moment gets the form:

$$P_D(\omega) = (\alpha_0 + \alpha_1 \cos(\Omega t))E_0 \cos(\omega t) \tag{3.2.1}$$

Writing out the cosine products gives:

$$P_D(\omega) = \alpha_0 E_0 \cos(\omega t) + \left(\frac{\alpha_1 E_0}{2}\right)[\cos((\omega+\Omega)\,t) + [\cos((\omega-\Omega)\,t)] \tag{3.2.2}$$

Apart from oscillating with a frequency ω (Rayleigh-scattering), the evanescing light will also oscillate with side-band frequencies $\omega+\Omega$ and $\omega-\Omega$, the Stokes and anti-Stokes side-bands respectively.

For crystals the susceptibility tensor χ_{jl} is used and the displacements of atoms are replaced by the normal coordinates Q_k of the oscillations. The susceptibility can be expanded with respect to the normal coordinates Q_k where the index k runs over all normal coordinates.

[1] (Devereaux & Hackl, 2007)

[2] (Kuzmany, 2009)

$$\chi_{jl} = (\chi_{jl})_0 + \sum_k \left(\frac{\partial \chi_{jl}}{\partial Q_k}\right)_0 Q_k + \sum_{k,m} \left(\frac{\partial^2 \chi_{jl}}{\partial Q_k \partial Q_m}\right)_0 Q_k Q_m + \dots \quad (3.2.3)$$

$\partial \chi_{jl}/\partial Q_k$ is a component of the derived polarizability tensor, or the so-called *Raman tensor*. This tensor is often written as $(\chi_{jl})_k$. The indexes j and l extend over the Cartesian coordinates 1 to 3. The index k runs over 3N-3 (N is number of atoms in the unit cell) normal coordinates. These coordinates are the optical modes probed with a wave vector **q**=0. When there is no phonon in the material an incoming **q**=0 photon can only generate a **k**=0 phonon in the centre of the Brillouin Zone by momentum conservation (and of course an outgoing **q**=0 photon is emitted) . Group theory allows to determine which vibrational species are Raman active. This is already calculated for every possible space group. The results can be found on specific sites.[1]

The intensity of scattered light is proportional to the square of the Raman tensor. Different elements of the Raman tensor can be probed by choosing the appropriate polarization geometries. The used geometry is conveniently written down in Porto notation: a(bc)d where the letters refer to the Cartesian coordinates of the crystal axes. a and d give the direction for the incident and scattered light. b and c the direction of the corresponding polarizations. The intensity for a certain polarization geometry is given as:

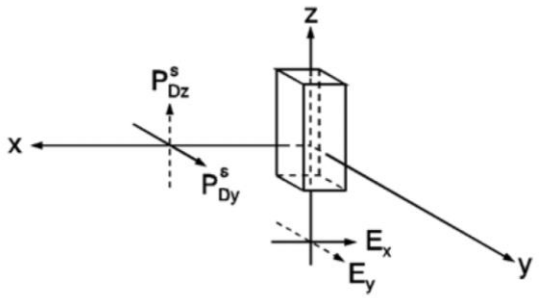

Figure 3-1 General picture of scattering geometry. For instance, the light comes in by the z-axis and scattered light is measured along the x-axis. When we use the dashed polarization of the EM-field this will give a scattering geometry z(yz)x.

$$I(\theta, R_T) = C' \left| \sum_{j,l} e_j^s \chi_{jl.k} e_l^i \right| E_0^2 \quad (3.2.4)$$

Raman scattering can of course also be thought of as a quantum-mechanical effect. Here an electron in an initial state **i** is excited by the incoming photon to a virtual state **z** (when **z** is a real state resonant Raman is possible). The electron relaxes back to a state **f** and to fulfill energy and momentum conservation the generation or absorption of an additional quasi-particle is required; the elementary excitation in a material we want to probe. To calculate the probability of the two optical transitions second-order perturbation theory is required. The process is depicted in Figure 3-2.

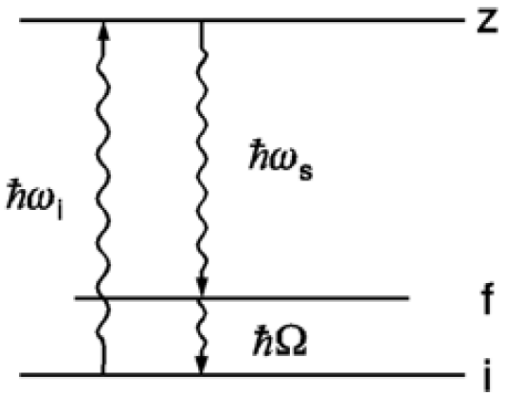

Figure 3-2 Quantum mechanical representation of Raman scattering.

[1] (Bilbao Crystallographic Server)

For a more lengthy discussion of Raman Spectroscopy I would refer to chapter 9 of Solid State Spectroscopy of H. Kuzmany[1]. The Raman selection rules are discussed in detail in chapter 8 of this book.

3.3 Electronic Raman scattering

3.3.1 General

This part describes the electronic continuum of the Raman spectrum upon which other excitations as phonons and magnons are superimposed. In electronic Raman scattering an electron is excited from an occupied state to an unoccupied state in a conduction band (nonresonant intraband scattering) which will be accompanied by the excitation of a photon. Another possibility is that an incoming photon excites the electron from a filled valence band to a partially filled conduction band. An electron from the conduction band will fall back to fill the unoccupied position in the valence band, which is again accompanied by the excitation of a energy-shifted photon (interband scattering). The excitations lying near the Fermi Surface are predominantly probed by the intraband scattering process. The capture of these processes in a theoretical model starts with a Hamiltonian for N electrons minimally coupled to an electromagnetic field given below:

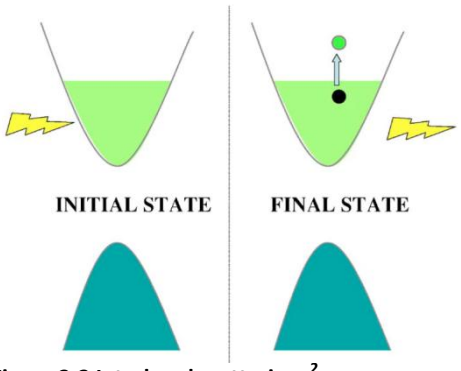

Figure 3-3 Intraband scattering. [2]

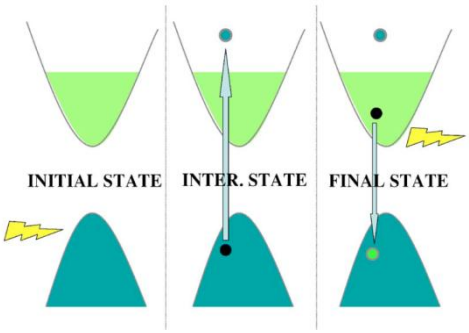

Figure 3-4 Interband scattering. [3]

$$H = \sum_{i}^{N} \frac{\left[\hat{\boldsymbol{p}}_i + \left(\frac{e}{c}\right)\hat{\boldsymbol{A}}(\boldsymbol{r}_i)\right]^2}{2m} \tag{3.3.1}$$

Here $\hat{\boldsymbol{p}}_i = -i\hbar\boldsymbol{\nabla}$ is the quantum mechanical momentum operator for the i[th] electron and $\hat{\boldsymbol{A}}(\boldsymbol{r}_i)$ the vector potential of the EM-field where the i[th] electron is positioned . m is the electron mass and e the elementary charge. The kinetic energy can be expanded as follows:

$$H = H' + \frac{e}{2mc}\sum_i [\hat{\boldsymbol{p}}_i \cdot \hat{\boldsymbol{A}}(\boldsymbol{r}_i) + \hat{\boldsymbol{A}}(\boldsymbol{r}_i) \cdot \hat{\boldsymbol{p}}_i] + \frac{e^2}{2mc^2}\sum_i \hat{\boldsymbol{A}}(\boldsymbol{r}_i) \cdot \hat{\boldsymbol{A}}(\boldsymbol{r}_i) \tag{3.3.2}$$

where

[1] (Kuzmany, 2009)

[2,3] (Devereaux & Hackl, 2007)

$$H' = \left(\frac{1}{2m}\right)\sum_i \hat{\boldsymbol{p}}_i{}^2 \tag{3.3.3}$$

The second and third terms in equation 3.3.2 acts as a perturbational Hamiltonian. The second term couples the electron's currents to a single photon and the third term couples the electron's charge to two photons. This gives the expression for the intraband and interband scattering. The polarization dependence comes in by the electromagnetic field operator $\widehat{\boldsymbol{A}}(\boldsymbol{r}_i)$:

$$\widehat{\boldsymbol{A}}(\boldsymbol{r}_i) = \sqrt{\frac{hc^2}{\omega_{\boldsymbol{q}} V}}[\hat{\boldsymbol{e}}_{\boldsymbol{q}} a_{-\boldsymbol{q}} + \hat{\boldsymbol{e}}_{\boldsymbol{q}}^* a_{+\boldsymbol{q}}^\dagger] \tag{3.3.4}$$

where the transversal photons with energy $\hbar\omega_{\mathbf{q}}$ have a polarization direction denoted by the complex unit vector $\mathbf{e}_{\mathbf{q}}$.

A general expression for the electronic scattering cross section is given via a transition rate R of scattering an incident ($\mathbf{q}_i$, ω_i,$\mathbf{e}_{\mathbf{q}}^{(i)}$) photon into a outgoing photon ($\mathbf{q}_s$, ω_s,$\mathbf{e}_{\mathbf{q}}^{(s)}$):

$$\frac{\partial^2\sigma}{\partial\Omega\partial\omega_s} = \hbar r_0^2 \frac{\omega_s}{\omega_i}\frac{1}{Z}\sum_{I,F} e^{-\beta E_I}\left|M_{F,I}\right|^2 \delta(E_F - E_I - \hbar\Omega) \tag{3.3.5}$$

Here $r_0{}^2 = e^2/mc^2$ is the Thomson radius, $\beta = 1/k_bT$, Z is the partition function and $M_{F,I} = < F|M|I >$ is the light-scattering operator expectation value as follows from the perturbation. $\Omega = \omega_i - \omega_s$ is the transferred energy and E_F and E_I the energies of initial and final state.

3.3.2 Polarization dependence, charge fluctuations and the Raman vertex

The polarization dependence of Raman scattering is classified using arguments of group theory. The big line of the story is that charge-density fluctuation brought about by light scattering are modulated in directions in momentum space determined by the polarization geometry. The charge density fluctuations have a symmetry imposed on them by the light orientation. The mathematical reasoning to this statement goes as follows:

The total transition matrix element $M_{F,I} = \sum M_I^\alpha M_F^\beta e_i^\alpha e_s^\beta$ can be decomposed in basis functions of the irreducible point group of the crystal.

$$M_{F,I}(\boldsymbol{q} \to 0) = \sum_\mu M_\mu \Phi_\mu \tag{3.3.6}$$

Here μ represents an irreducible representation of the point group of the crystal and Φ_μ the accompanying basis function.

These basis functions belonging to a certain irreducible representation and polarization geometry are linear expansions of the *Raman vertices* which are on itself directly proportional to the *effective charge fluctuations*. The charge fluctuations give how charge fluctuates under a certain symmetry in momentum space or in the Brillouin Zone:

$$\hat{\rho}(\boldsymbol{q}) = \sum_{\alpha,\beta} \gamma_{\alpha,\beta}(\boldsymbol{k},\boldsymbol{q}) c^{\dagger}_{\boldsymbol{k}+\boldsymbol{q},\sigma} c_{\boldsymbol{k},\sigma} \tag{3.3.7}$$

This charge density fluctuation is a sum over the annihilation of electronic states **k** and the creation of state **k+q** (as an photon with momentum **q** is absorbed) weighted by scattering amplitudes. Here α and β refer to incoming and outgoing polarizations. The Raman scattering rate is proportional to the amount of *charge fluctuation* $\hat{\rho}(\boldsymbol{q})$ probed. In a second quantized form one talks about a *vertex* to describe the interaction strength.

The vertices γ(k) or the basis functions Φ_μ itself can be expanded in spherical harmonics $Y_m^l(\theta,\varphi)$ which determine the direction of the charge fluctuation in **k**-space. The $Y_m^l{}'s$ are the angular part of a wave function under the full rotational group. As one works with a specific symmetry group, appropriate boundary solutions must be imposed to give a linear expansion of $Y_m^l{}'s$ to form the basis functions Φ_μ which transform according to the right symmetry group. The basis functions Φ_μ go by the name *crystal harmonics, Brillouin Zone harmonics* or *Fermi surface harmonics* in literature according to the taste of the author. The crystal harmonics for the D_{4h}-type space groups are given by Table 3-1.This table is also applicable to the ferropnictides as they also belong to the D_{4h}-type space groups.

Geometry	$\hat{e}_i$	$\hat{e}_s$	R	Basis functions $\Phi_\mu(\mathbf{k})$
$xx,\ yy$	$\hat{x},\hat{y}$	$\hat{x},\hat{y}$	$R_{A_{1g}}+R_{B_{1g}}$	$\frac{1}{2}[\cos(k_x a)+\cos(k_y a)]\pm\frac{1}{2}[\cos(k_x a)-\cos(k_y a)]$
$x'x'$	$\frac{1}{\sqrt{2}}(\hat{x}+\hat{y})$	$\frac{1}{\sqrt{2}}(\hat{x}+\hat{y})$	$R_{A_{1g}}+R_{B_{2g}}$	$\frac{1}{2}[\cos(k_x a)+\cos(k_y a)]+\sin(k_x a)\sin(k_y a)$
$x'y'$	$\frac{1}{\sqrt{2}}(\hat{x}+\hat{y})$	$\frac{1}{\sqrt{2}}(\hat{x}-\hat{y})$	$R_{B_{1g}}+R_{A_{2g}}$	$\frac{1}{2}[\cos(k_x a)-\cos(k_y a)][1+\sin(k_x a)\sin(k_y a)]$
xy	$\hat{x}$	$\hat{y}$	$R_{B_{2g}}+R_{A_{2g}}$	$\sin(k_x a)\sin(k_y a)\left\{1+\frac{1}{2}[\cos(k_x a)-\cos(k_y a)]\right\}$
LR	$\frac{1}{\sqrt{2}}(\hat{x}+i\hat{y})$	$\frac{1}{\sqrt{2}}(\hat{x}+i\hat{y})$	$R_{B_{1g}}+R_{B_{2g}}$	$\frac{1}{2}[\cos(k_x a)+\cos(k_y a)]+\sin(k_x a)\sin(k_y a)$
LL	$\frac{1}{\sqrt{2}}(\hat{x}+i\hat{y})$	$\frac{1}{\sqrt{2}}(\hat{x}-i\hat{y})$	$R_{A_{1g}}+R_{A_{2g}}$	$\frac{1}{2}\{\cos(k_x a)+\cos(k_y a)+[\cos(k_x a)-\cos(k_y a)]\sin(k_x a)\sin(k_y a)\}$
xz	$\hat{x}$	$\hat{z}$	$R_{E_{1g}}$	$\sin(k_x a)\sin(k_z c)$
yz	$\hat{y}$	$\hat{z}$	$R_{E_{1g}}$	$\sin(k_y a)\sin(k_z c)$
zz	$\hat{z}$	$\hat{z}$	$R_{A_{1g}}$	$\cos(k_z c)$

Table 3-1 The Brillouin Zone harmonics for the D_{4h} space groups as found in Devereaux&Hackl. xy refers to the crystal axes (for $Ba(Fe_{1-x}Co_x)_2As_2$ this is ab) and x'y' (for $Ba(Fe_{1-x}Co_x)_2As_2$ this is xy) to the 45° rotated axes.

As discussed, the crystal harmonic essentially acts as a weight factor to the scattering intensity. For instance, for a crossed x'y'-polarization geometry transforming as B_{1g} light (Figure 3-5) will couple to charge excitations along the Brillouin Zone axes where $k_x = 0$ and k_y:0 → π/a or vice versa. Here the $\Phi_\mu(k)$ basis function will be nonzero, hence giving a maximal weight and nonzero intensity. The xy-geometry will project the parts along the Brillouin Zone axes where $k_x = \pm k_y$ (Figure 3-5). Single

symmetry element responses can be obtained by proper subtraction of scattering intensities of different polarization geometries.

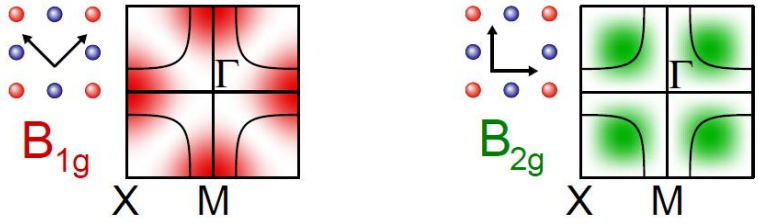

Figure 3-5 Different polarization geometries probe different Brillouin Zone parts. [1]

This is what Raman Spectroscopy makes a method which can probe different parts of the Brillouin Zone by just simply choosing the right polarization configuration. As there are bands located at different high symmetry points in the Brillouin Zone, Raman scattering can probe electron dynamics on different bands.

3.3.3 Raman intensity final form

With this knowledge we can go back to equation 4.3.5. In the limit of small momentum transfer $\mathbf{q} = \mathbf{q}_i - \mathbf{q}_f$, $\mathbf{q} \to 0$ and some further manipulations as explained in *Devereaux&Hackl* the following form of the Raman scattering intensity is found:

$$\frac{\partial^2\sigma}{\partial\Omega\partial\omega_s} = \hbar r_0^2 \frac{\omega_s}{\omega_i}\hat{S}(\boldsymbol{q}, i\Omega \to \Omega + i0) \tag{3.3.9}$$

Here $\hat{S}$ is the Raman effective density-density correlation function which includes the effective charge density $\hat{\rho}$ from formula 4.3.7 where the photons scatter off:

$$\hat{S}(\boldsymbol{q}, i\Omega) = \sum_I \frac{e^{-\beta E_I}}{Z}\int d\tau\, e^{i\Omega\tau} < F|T_\tau\hat{\rho}(\boldsymbol{q},\tau)\hat{\rho}(-\boldsymbol{q},0)|I > \tag{3.3.10}$$

A trivial temperature dependence can be stripped off of the effective density-density correlation function according to:

$$\hat{S}(\boldsymbol{q},\Omega) = -\frac{1}{\pi}\{1 + n(\Omega,T)\}\hat{\chi}''(\boldsymbol{q},\Omega) \tag{3.3.11}$$

where $n(\Omega, \mathrm{T})$ is the Bose-Einstein distribution. This leaves $\hat{\chi}''(\boldsymbol{q},\Omega)$ as the bare Raman response or susceptibility as published in articles. This $\hat{\chi}''(\boldsymbol{q},\Omega)$ can be modelled for single-particle excitations but also for correlated particles as a Cooper pair. The $\hat{\chi}''(\boldsymbol{q},\Omega)$ response for breaking of a Cooper pair will be discussed later on in this chapter in paragraph 3.4.

Correction terms to $\hat{\chi}''(\boldsymbol{q},\Omega)$ can arise by including Coulomb interaction between particles. Other correction terms can arise by the specific shape of a band (parabolic/nonparabolic).

[1] (Devereaux & Hackl, 2007)

3.4 Electronic Raman Scattering in the superconducting state

3.4.1 The Tsuneto-Maki response function

In chapter *II.D. 3. Interacting electrons – nonresonant response* and *II.D. 6. Superconductivity* in Devereaux' article *Inelastic light scattering from correlated electrons* a lengthy derivation for the Raman intensity in the superconducting state is made. First a general expression for correlated electrons is derived in *II.D.3*. This expression gives the Raman intensity for correlated electrons as a convolution of the Raman vertex and a Greens propagation function. *In II.D.6* the Greens function for the superconducting state (BCS expression) comes in. The end result of this lengthy derivation is stated below[1,2] :

$$\chi_{\hat{\rho},\hat{\rho}}(\omega) = \frac{1}{N}\sum_{\boldsymbol{k}}\sum_{n}\gamma_n(\boldsymbol{k})^2\lambda_n(\boldsymbol{k},\omega) \tag{3.4.1}$$

This is the Raman response for n bands crossing the Fermi level. This is the bare Raman response which does not include correction terms due to Coulomb screening and charge backflow as explained before. This is the *total* electronic Raman response coming from *all* bands. Responses of different bands can be accessed by choosing the appropriate polarization components as we know from above.

$\lambda_n(\mathbf{k}, \omega)$ is the so-called Tsuneto-Maki function for the n^{th} band in the material:

$$\lambda_n(\boldsymbol{k},\omega) = \tanh\left(\frac{E_n(\boldsymbol{k})}{2k_BT}\right)\frac{4|\Delta_n(\boldsymbol{k})|^2/E_n(\boldsymbol{k})}{4E_n^2(\boldsymbol{k}) - (\hbar\omega + i\delta)^2} \tag{3.4.2}$$

The band dispersion relation is given as $\varepsilon_n(\mathbf{k})$ and the superconducting gap around the n^{th} band as $\Delta_n(\mathbf{k})$. The quasiparticle energy is given by $\mathrm{E}_\mathrm{n}^2(\mathbf{k}) = \varepsilon_\mathrm{n}^2(\mathbf{k}) + \Delta_\mathrm{n}^2(\mathbf{k})$. The imaginary part of $\lambda_n(\boldsymbol{k},\omega)$ gives the Raman response in the superconducting state at T=0K:

$$Im\,\chi_{\hat{\rho},\hat{\rho}}(\omega) = \sum_n Im\,\chi^n_{\hat{\rho},\hat{\rho}}(\omega) = \sum_n \frac{\pi N_{F,n}}{\omega} Re\int d\theta\,\gamma_n^2(\theta)\,\frac{|\Delta_n(\theta)|^2}{\sqrt{\omega^2 - 4|\Delta_n(\theta)|^2}} \tag{3.4.3}$$

Different responses to this formula will be discussed below.

3.4.2 Responses for different gap function symmetries

The response function above is evidently responsible for the pair breaking peak at $\omega=2\Delta(\theta)$ as the denominator goes to zero. When the denominator goes to zero there will be a divergent response.

This is the way one can determine the symmetry of the gap function. In the case for an isotropic gap $\Delta(\theta)=\Delta$ (s-wave) there should always be a divergence at a Raman shift $\Omega=2\Delta$ rounded off by scattering. The same goes for a $s^{\pm}$-wave as one cannot measure phase with Raman.

[1] (Devereaux & Hackl, 2007), page 193, page 197-198

[2] (Boyd & Devereaux, Probing the pairing symmetry of the iron pnictides with electronic Raman scattering, 2009)

For the more exotic gap functions (as described in 2.5 Superconducting properties) there will still be a pair breaking peak located at $2\Delta_0$, but also Cooper pairs with a smaller gap will be broken. This will give a divergence. As the gap function is continuous, this will give rise to a continuous spectrum of broken Cooper pairs with different pairing energies.

When there will still be a finite electronic Raman signal in the superconducting state at a shift Ω=0, Cooper pairs with a gap energy Δ=0 meV are broken. This means that there is a node around the Fermi surface in the gap function, hence a d-wave symmetry around the probed band. Of course one cannot measure up to Ω=0, this needs to be done by extrapolating the signal.

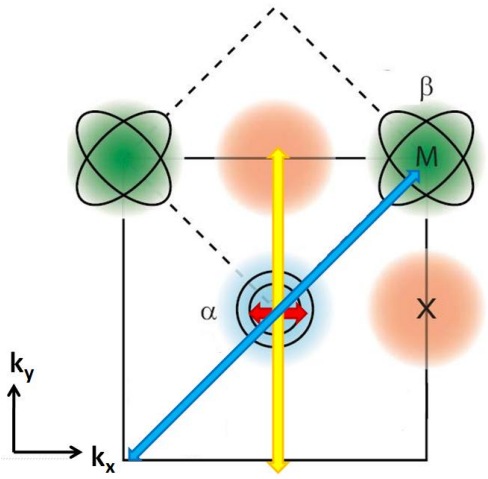

Figure 3-6 Some possibilities for breaking Cooper pairs (red, yellow, blue arrows) at different bands in the BZ of $Ba(Fe_{1-x}Co_x)_2As_2$.

When the measured signal has a slope and extrapolation of the electronic signal gives a crossing of the Raman shift-axis at zero intensity, this will mean that the intensity at Ω=0 is I(Ω=0)=0, so no Cooper-pairs with a gap of Δ=0 meV are broken. By this fact and the slope of the signal one can conclude that the gap function is an anisotropic s-wave. Cooper pairs with different *nonzero* gap energies are broken.

As one knows formula 3.4.3 this leaves the opportunity to *calculate* a Raman spectrum in the superconducting state and to compare it to experimental data. *Muschler et al.* did this for $Ba(Fe_{0.939}Co_{0.061})_2As_2$. The responses for crossed polarization geometry B_{2g} and circular polarization A_{1g} are presented. The A_{1g} spectrum in (a) crosses the zero intensity line at a finite Raman shift Ω. Furthermore, the SC spectrum isn't flat. This gives an anisotropic s-wave around the bands at the Γ-point according to the reasoning above. There is a broad maximum at $100cm^{-1}$. Below $80cm^{-1}$ the A_{1g} spectrum varies as $\Omega^{1.6}$. Extrapolating this relation will result in a threshold value of $\Delta_{min} \leq 2meV$ for the Cooper pairs.

The B_{2g} spectrum shows a clear peak around $70cm^{-1}$. Here a $\Omega^{0.5}$ relation is found. Extrapolating this curve will result in a finite intensity at $\Omega=0$. This hints at the presence of nodes around the Fermi surface of the band at the M-point. A summary of their results is given in (c) . Plot (d) shows the theoretical spectra calculated using the Tsuneto-Maki function.

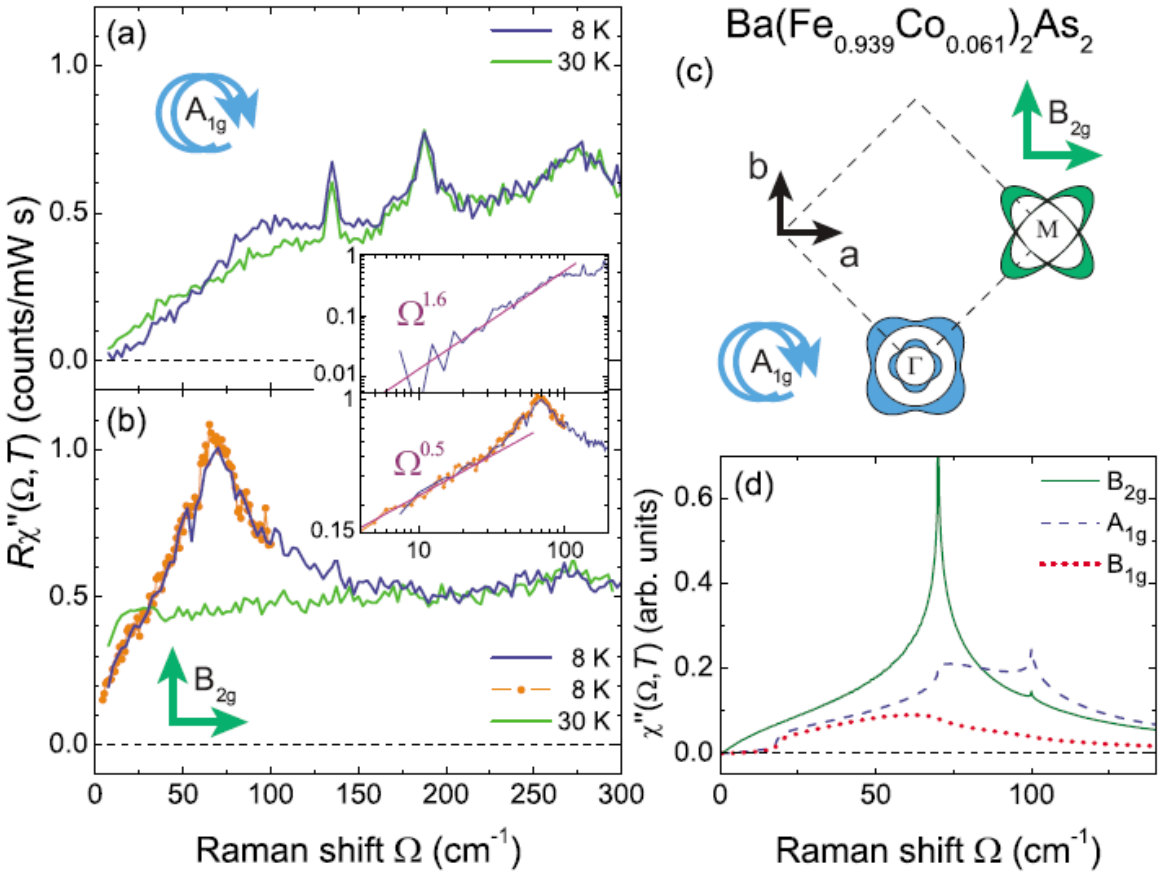

Figure 3-7 The results of Muschler et al. The A_{1g} and B_{2g} spectra are shown. In these spectra they noticed a clear change in scattering in the SC-state. An anisotropic s-wave around the α-band was found, around the β-band a d-wave was found.

3.4.3 Final-State interaction correction

Authors of experimental articles on Raman scattering on high-T_c superconductors generally refer to a correction term which needs some simple clarification. This term goes by the name *Final-state interaction*.

When a Cooper pair is broken into two electrons there will also be two holes created. There can still be an attraction between these particles which does not contribute anymore to the reformation of the Cooper pair, the so-called *residual interaction.* This will give rise to a four-body problem. The bound pairs in this final state can have an electron-electron, hole-hole or electron-hole character. Also these new bound pairs are probed by Raman scattering, but this small continuous spectrum *above* 2 Δ is too small to be experimentally resolved as it will vanish under the broadened Cooper pair breaking peak. More about Raman scattering in the Final-State can be found in an article by *H. Monien and A. Zawadowski*.[1]

[1] (Monien & Zawadowski, 1990)

4 Experimental

4.1 Setup

The two different setups used will be discussed in this paragraph; *micro-Raman* and *macro-Raman*. The first part of the beam line as shown in Figure 4-1 is the same for both setups.

The Verdi V6 λ=532nm laser was used as an excitation source. A grey filter was put in the beam line to lower the intensity selectively. The band filter was placed to eradicate a fluorescing signal originating in the laser which else showed up in the Raman spectrum. The two following dichroic mirrors allow to optimize the signal in the micro setup. In the macro setup these mirrors are not critical for the alignment anymore.

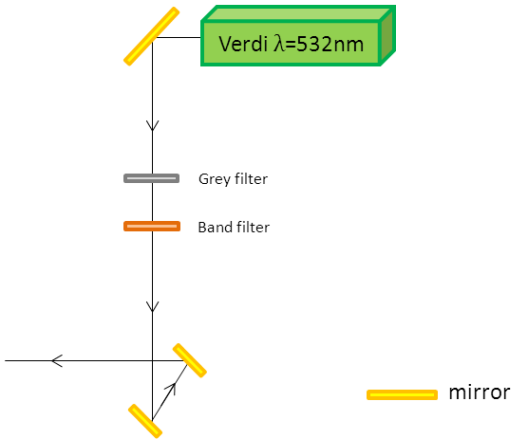

Figure 4-1 First part of optical path as seen from above.

4.1.1 Micro

The micro setup as seen from above is shown in Figure 4-2. The incoming beam has a diameter Ø=3mm. It passes through a f=20mm lens where after it goes through a beam splitter and a f=50mm lens. The beam goes through a Olympus LM Plan FL 50x/0.50 microscope to illuminate the sample to give a *backscattering configuration*. The opening angle of the microscope is 30°. A long focal distance for the microscope is necessary to reach the sample when it is placed in the cryostat. The scattered signal goes through a pinhole which blocks out-of-focus scattered light and mostly only lets through signal from the focus point. An f=200mm lens makes the beam parallel again. Different polarization components of the scattered light can be selected out by the polarizer and a λ/2 which rotates the light over 90°. This is necessary as the monochromator is way more sensitive to vertically polarized light as horizontal polarized light.

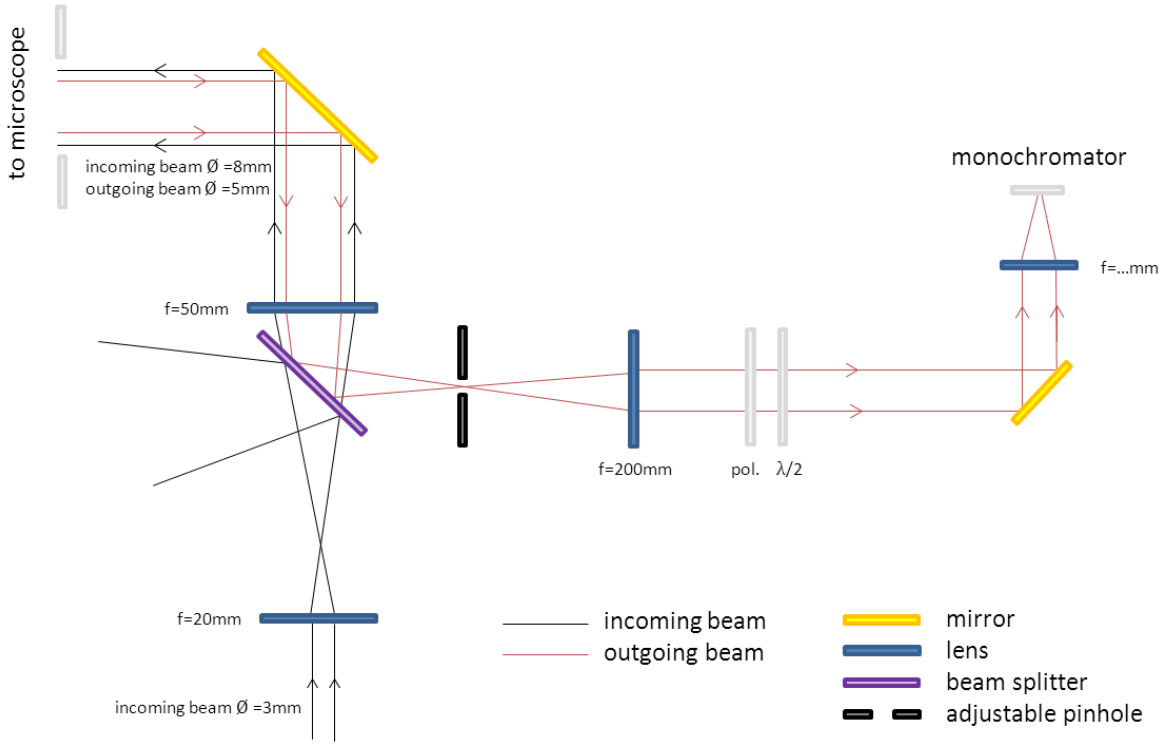

Figure 4-2 Micro setup[1]

Confocal microscopy is used in the setup. The principle of how out-of-focus intensity is blocked by the pinhole is depicted in Figure 4-3. The more closed the pinhole is, the better the resolution will be.

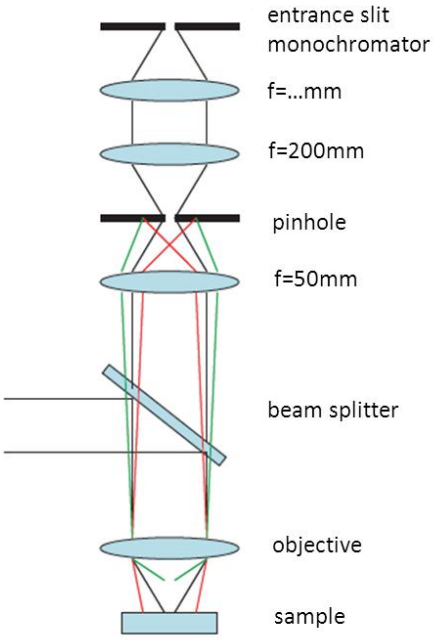

Figure 4-3 Confocal microscopy setup[2]

[1] Illustration from micro setup. Adapted by R.B. Versteeg from drawing by B. Hesp

[2] Illustration adapted from (Fausti, 2008), page 92/161

4.1.2 Macro

The macro setup depicted in Figure 4-4 has three mirrors which deform the incoming beam. The incoming beam is focused on the sample by an f=15cm lens. As the beam impinges on the sample under a finite angle of about 60° the laser spot will be deformed to an elliptical shape. A 60° angle was chosen to be around the Brewster angle. A great part of the incoming laser intensity is directly reflected out of the cryostat. The Raman signal and some incoherent scattering will be collected by a two-lens system coupled into the monochromator. This 2-lens system is composed of a f=55mm collection lens and a f=25cm lens. This system will magnify the imaged sample and project it on the entrance slit. A crude estimation for the magnification factor $M = f_2/f_1 = 25cm/5.5cm \approx 4.5$ follows for the lens-system.

The macro setup was just a trial setup to probe the phonons in the material. Not much attention was paid to optimize the collection of signal and selection rule breaking.

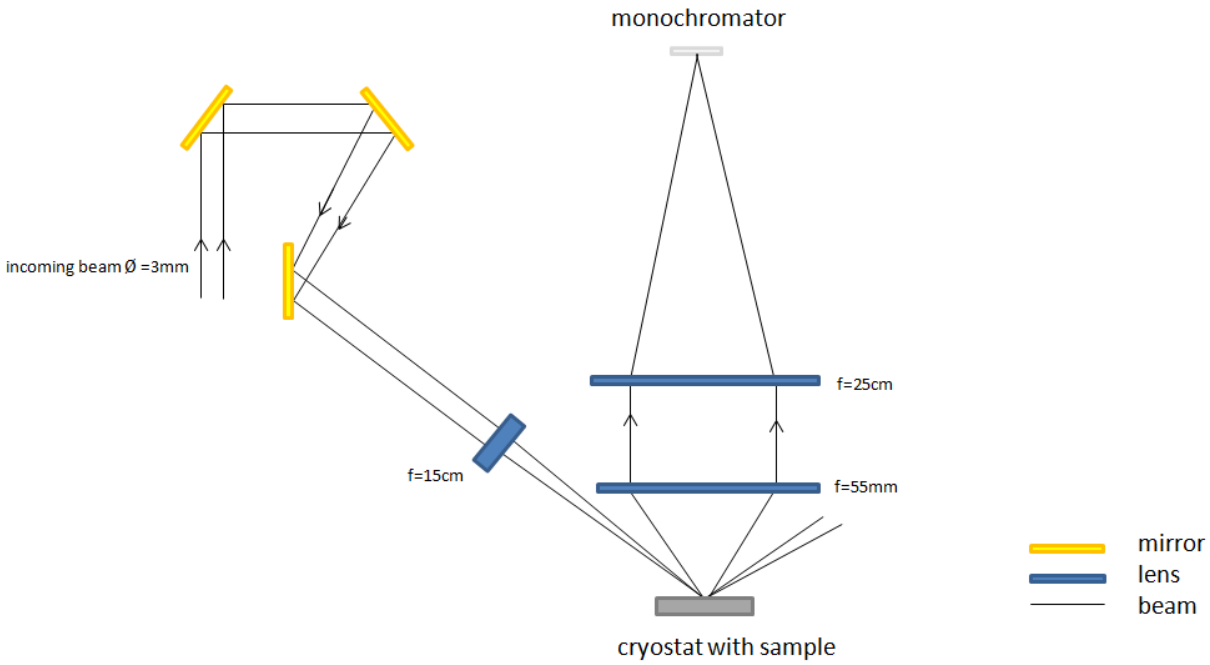

Figure 4-4 Macro setup[1]

[1] Illustration made by R.B. Versteeg

4.1.3 Monochromator

The triple-grating monochromator T64000 by Jobin Yvon was used. It is equipped with a liquid nitrogen cooled CCD by Horiba.

An impression of the working of a triple grating monochromator is given in Figure 4-5. The first grating spatially disperses the light so that the first intermediate slit can select the wavelength region to be investigated. The second grating recombines the wavelength region and images the entrance slit on the second slit. In a different chamber in the monochromator housing the light is once more dispersed by the third grating on the CCD camera.

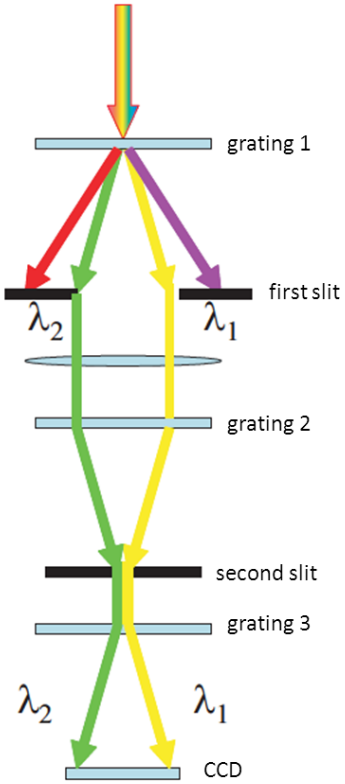

Figure 4-5 Illustration of the working of a triple grating monochromator.[1]

4.1.4 Cryostat

An Oxford-Instruments cryostat with allowed temperature ranging from 3K to 320K was used. The stability of the cryostat is ±0,1K. The sample is cooled with liquid helium.

When the sample is placed in the cryostat the intensity with respect to outside the cryostat will drop by a factor 3. The reason for this is still an unresolved problem.

4.2 Used material

The material studied for this bachelor thesis is the 122-compound $BaFe_{1.80}Co_{0.20}As_2$ so the nominal cobalt-doping is x=0,10 ($Ba(Fe_{1-x}Co_x)_2As_2$). The true cobalt-doping varies between x= 0.165 and x=0.17. This gives a transition temperature around $T_c \approx 22K$. The sample has a silver shiny appearance and was grown by the Van der Waals – Zeeman Institute of the University of Amsterdam.

4.2.1 Space group considerations

According to [2] there are 5 Raman active modes for the P4/mmm group or no. 139 group: A_{1g}, B_{1g}, B_{2g} and two E_g modes. The 5 Raman Tensors are given below:

[1] Illustration adapted from (Fausti, 2008), page 92/161

[2] (Bilbao Crystallographic Server)

$$A_{1g}: \begin{bmatrix} a & 0 & 0 \\ 0 & a & 0 \\ 0 & 0 & b \end{bmatrix} \qquad B_{1g}: \begin{bmatrix} c & 0 & 0 \\ 0 & -c & 0 \\ 0 & 0 & 0 \end{bmatrix} \qquad B_{2g}: \begin{bmatrix} 0 & d & 0 \\ d & 0 & 0 \\ 0 & 0 & 0 \end{bmatrix}$$

(4.2.1)

$$E_g: \begin{bmatrix} 0 & 0 & 0 \\ 0 & 0 & e \\ 0 & e & 0 \end{bmatrix} \qquad E_g: \begin{bmatrix} 0 & 0 & -e \\ 0 & 0 & 0 \\ -e & 0 & 0 \end{bmatrix}$$

Crossed and parallel scattering configurations were used in the quasi-backscattering micro-setup. The scattering configuration is given in Porto notation: c(ab)c. This means that the sample is illuminated along the crystals c-axis with the electric field parallel to the crystal a-axis. From the backscattered light the component with the electric field parallel to the b-axis is measured. This is done by choosing the appropriate polarizations. The xy-axis-system can be probed by rotating the sample 45°. The a-axis and b-axis are parallel to the Fe-As-Fe-bindings as was seen Figure 2-8 in section 2.4.

The nonzero electronic transition rates and their corresponding polarizations can be determined according to table I in section 3.3.2. As A_{2g} isn't a Raman active mode for the P4/mmm group $R_{A_{2g}} = 0$ and is not included below. Furthermore, as the sample is illuminated along the c-axis, the E_g channels are also not probed. This table gives the following bands probed by different geometries.

Used geometry	Scattering rate	Probed bands	Character probed bands
c(aa)c	$R_{A_{1g}} + R_{B_{1g}}$	α,γ,δ	Hole and electron
c(ab)c	$R_{B_{2g}}$	β	Hole
c(xx)c	$R_{A_{1g}} + R_{B_{2g}}$	α,β	Hole
c(xy)c	$R_{B_{1g}}$	δ,γ	Electron

Table 4-1 Geometry vs. probed bands.

The folded Brillouin Zone, the bands, the specific symmetry channels and the used polarization geometries are depicted in Figure 4-6.

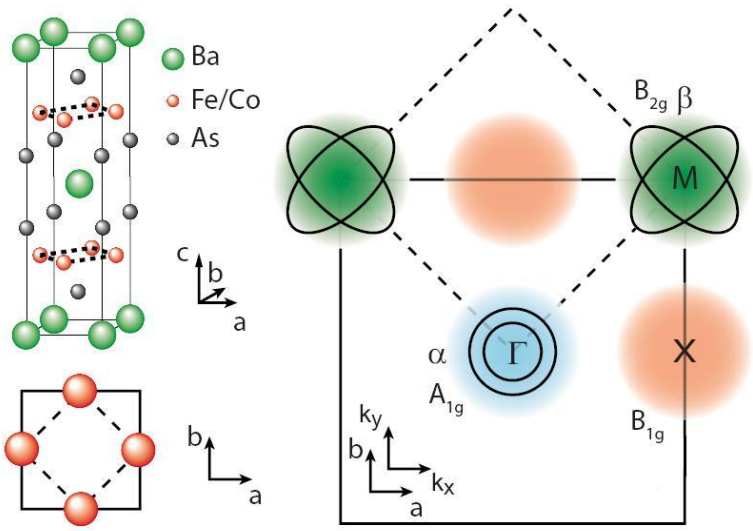

Figure 4-6 On the left the unit cell of $Ba(Fe_{1-x}Co_x)_2As_2$ is shown with the iron arsenide plane and crystal axes. On the right the folded Brillouin Zone is shown with the used experimental polarization geometries, symmetry channels and probed bands.

As an example of how to determine these transition rates, consider the c(xx)c –spectrum. The accompanying crystal harmonic is

$$\Phi_k(\boldsymbol{k}) = \frac{1}{2}\left[\cos(k_x a) + \cos\left(k_y a\right)\right] + \sin(k_x a)\sin\left(k_y a\right) \qquad (4.2.2)$$

The weight factor at (k_x, k_y)=(0,0) is {½(1+1)+0}=1 so the the α-band or hole band at the center of the Brillouin Zone is probed. At (k_x, k_y)=(0,±π/a) and (±π/a,0) the weight factor is given as {(1/2)(1-1) + 0} = 0 so the γ and δ electron bands aren't probed. At the (k_x, k_y)=(+π/a,+π/a) points the weight factor is 2 so the β-band or hole band is probed, etcetera.

5 Results and discussion

5.1 Phonons

From the above symmetry considerations in and the atoms position in the unit cell one expects four Raman active phonons for $Ba(Fe_{1-x}Co_x)_2As_2$ [1]:

1. An A_{1g} phonon due to the vibration of As atoms along the c-axis.
2. An B_{1g} phonon due to the vibration of Fe atoms along the c-axis.
3. A low frequency E_{1g} phonon mixed mode due to displacements of both Fe and As atoms in the FeAs-plane.
4. A high frequency E_{1g} phonon mixed mode due to displacements of both Fe and As atoms in the FeAs-plane.

Symmetry breaking of the unit cell by doping with cobalt can give rise to other vibrational modes, for instance Co-As modes and Fe-Co modes.

As can be seen from the Raman tensors, crossed and parallel polarization geometries with the sample illuminated along the c-axis will only probe A_{1g} and B_{1g} phonons.

5.1.1 Angular dependence phonons

An angular dependence was done to determine the orientation of the sample. As the sample is illuminated along the c-axis, there is no polarization component in this direction. Only the a_{11} , a_{12}, a_{21} and a_{22} elements of the Raman tensors contribute to the intensity The scattering intensity from mode R_T when the sample is θ degrees off-axis:

$$I(\theta, R_T) = C' \left| \sum_{j,l} e_j^s R^{-1}(\theta) R_{jl,T} R(\theta) e_l^i \right| E_0^2 \tag{5.1.1}$$

Here e_j^s and e_l^i are the scattered and incoming polarizations. $R^{-1}(\theta)$ and $R(\theta)$ are Euler-rotation matrices where θ is the angle in the ab/xy-plane.

The rotated A_{1g} and B_{1g} tensors are:

$$R^{-1}(\theta) A_{1g} R(\theta) = \begin{bmatrix} a & 0 \\ 0 & a \end{bmatrix} \tag{5.1.2}$$

$$R^{-1}(\theta) B_{1g} R(\theta) = \begin{bmatrix} c(cos2\theta) & c(sin2\theta) \\ c(sin2\theta) & -c(cos2\theta) \end{bmatrix} \tag{5.1.3}$$

Jones vectors are used to mathematically model the polarization components with respect to the ab/xy-axes:

$$\hat{a} \rightarrow \begin{pmatrix} 1 \\ 0 \end{pmatrix} \qquad \hat{b} \rightarrow \begin{pmatrix} 0 \\ 1 \end{pmatrix} \qquad \hat{x} \rightarrow \frac{1}{\sqrt{2}} \begin{pmatrix} 1 \\ 1 \end{pmatrix} \qquad \hat{y} \rightarrow \frac{1}{\sqrt{2}} \begin{pmatrix} 1 \\ -1 \end{pmatrix} \tag{5.1.4}$$

[1] (Bilbao Crystallographic Server; Bilbao Crystallographic Server)

Putting the rotated matrices between the incoming and outgoing polarization vectors gives the angular dependency of a Raman mode for the experimental polarization geometries:

Used geometry	$(I(\theta, A_{1g}) \sim$	$I(\theta, B_{1g}) \sim$
c(aa)c	a^2	$c^2 \cos^2(2\theta)$
c(ab)c	0	$c^2 \sin^2(2\theta)$
c(xx)c	a^2	$c^2 \sin^2(2\theta)$
c(xy)c	0	$c^2 \cos^2(2\theta)$

Table 5-1 Angular dependency intensity of phonon modes

A small guide for the eye for these intensities is shown below:

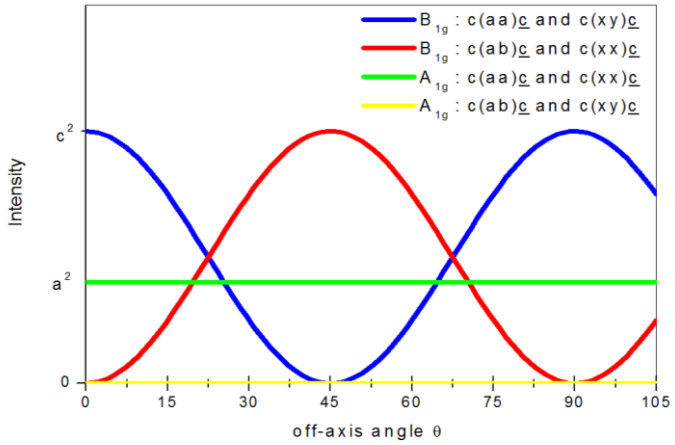

Figure 5-1 Angular dependence of A_{1g} and B_{1g} phonons in the used scattering geometries.

The experimental dependence in crossed polarization geometry is seen in Figure 5-2. The angle was measured with respect to the copper plate on which the sample was glued.

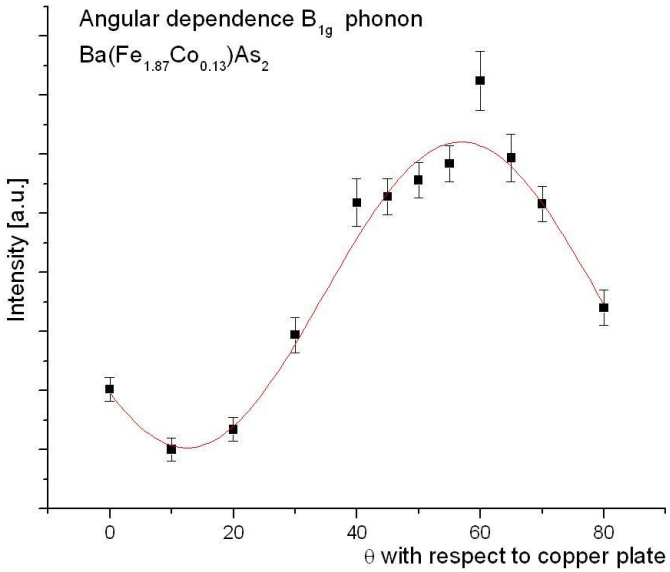

Figure 5-2 Experimental angular dependence of the B_{1g} phonon.
The maximum is around 55 degrees and gives the xy-axes of the crystal.

5.1.2 The B_{1g}-phonon

The B_{1g} phonon shifts from (211±2) cm^{-1} to (216±2) cm^{-1} upon cooling from T=295K to T=5K. Furthermore a sharpening of the peak can be observed. The +5 cm^{-1} suggests that the B_{1g} phonon is a hard phonon. The B_{1g} phonon-mode is associated with the displacement of Fe atoms along the c-axis. This gives that the c-axis lattice parameter contracts upon cooling giving a bigger elastic constant hence a bigger Raman shift.

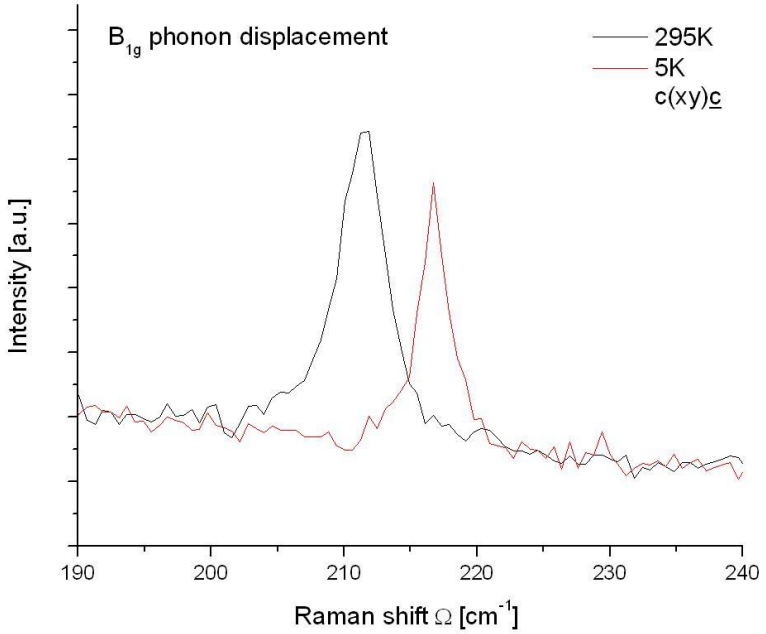

Figure 5-3 Shift of B_{1g} phonon upon cooling shows that the B_{1g} phonon is a "hard phonon".

From the angular dependence measurements a count rate of (0,11±0,01) cnt s^{-1} mW^{-1} for the B_{1g} phonon in optimal configuration at room temperature follows. This was determined in the micro setup. For comparison, the silicon 520cm^{-1} mode count rate is around 200 cnt s^{-1} mW^{-1}.

5.1.3 The A_{1g}-phonon

After the angular dependence was done the sample was placed in the correct position to measure the c(xx)c -spectrum. Here the A_{1g} phonon should be visible irrespective of sample orientation (see angular dependency A_{1g} mode). Contrary to what was expected, the A_{1g} phonon was not found on the studied sample in micro. 4 measurements of 30 minutes at T=4K were made and 4x30minutes of measurements at T= 30K (above T_c) were made with an intensity of (0,50±0,05)mW illuminating the sample to outrule the possibility of heating the sample.

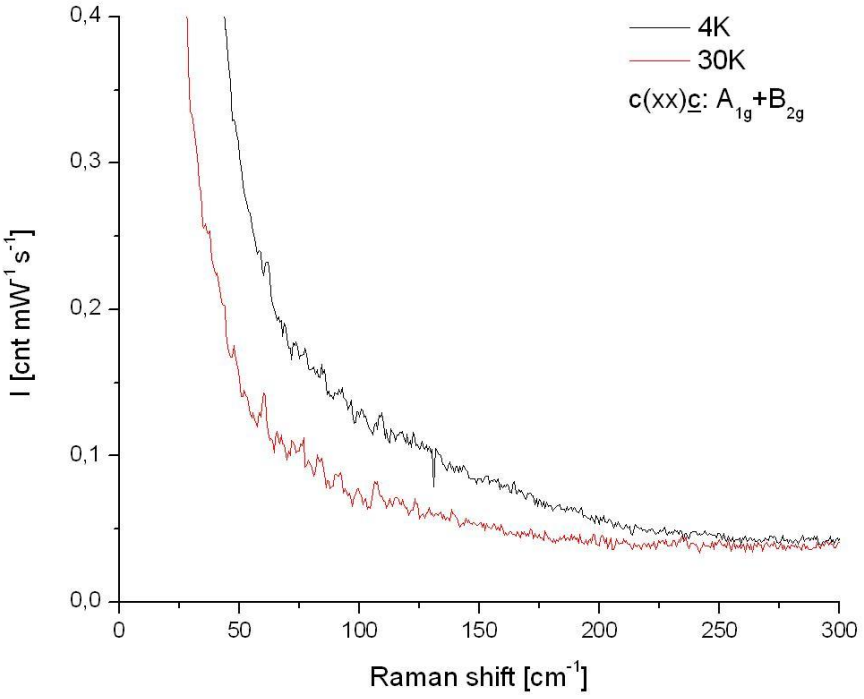

Figure 5-4 The A_{1g} phonon didn't show up at low temperatures in micro.

An angular dependence in parallel polarization geometry was made by A. Caretta on an "old" $BaFe_{1.87}Co_{0.13}As_2$ sample before this bachelor project. Here the A_{1g} phonon also didn't show up. Here the excitation wavelength was λ=647nm.

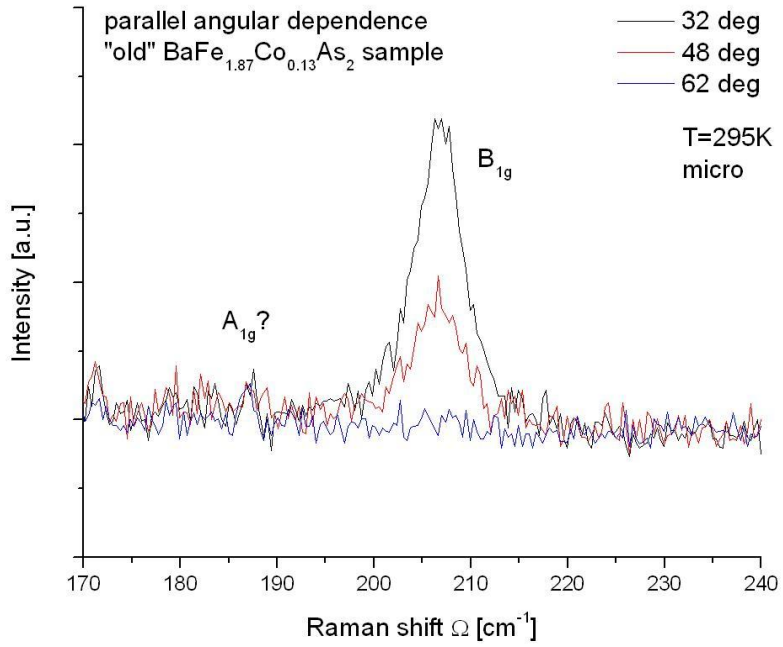

Figure 5-5 Angular dependence on "old" sample measured in parallel polarization geometry didn't give the A_{1g} phonon.

Muschler only presents 8K and 30K spectra. Here the A_{1g} phonon shows up in the A_{1g} spectrum around Ω=185cm^{-1} probed with right handed circular incoming polarization and right handed circular outcoming polarization. Sugai found a clearly resolvable A_{1g} phonon around Ω=185cm^{-1} with a height about equal to the B_{1g} phonon (due to leakage of polarizing components) in the c(xx)c̲-spectrum at room temperature with an excitation wavelength of λ=514,5nm. Here the same polarization geometry as in our experiment was used except for that these spectra are measured in macro as was realized later on due to the missing of the Rayleigh-wing scattering and the argument below.

As a first possible explanation for the absence of the A_{1g} phonon it was thought that the a-elements of the A_{1g} Raman tensors are very small with respect to the a_{33}=b element. As the micro-setup doesn't have a z-component in the incoming polarization, the a_{33}=b element isn't probed.

$$A_{1g}: \begin{bmatrix} a & 0 & 0 \\ 0 & a & 0 \\ 0 & 0 & b \end{bmatrix}$$

To probe the b element the macro setup was placed with the incoming beam under an angle of about 60°. In this way the illuminating electromagnetic field has a finite projection of the polarization along the c-axis and the b element of the A_{1g} Raman tensor will also be weighted. Room temperature c(xy)c̲- and c(xx)c̲-spectra were measured in macro as shown in Figure 5-7. Still no clear A_{1g} was found at room temperature, at least not an A_{1g} phonon mode with an intensity about equal to the B_{1g} phonon as found by *Sugai et al*.

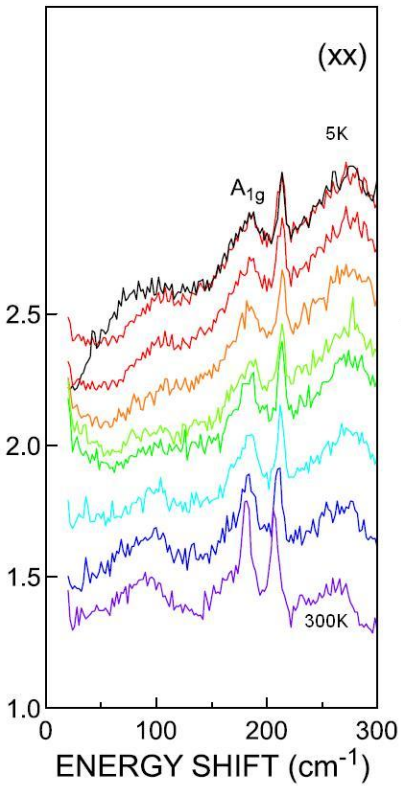

Figure 5-6 c(xx)c̲-spectrum by Sugai on $BaFe_{1.84}Co_{0.16}As_2$. The A_{1g}-phonon is clearly resolved at Ω=185cm^{-1} at T=300K.

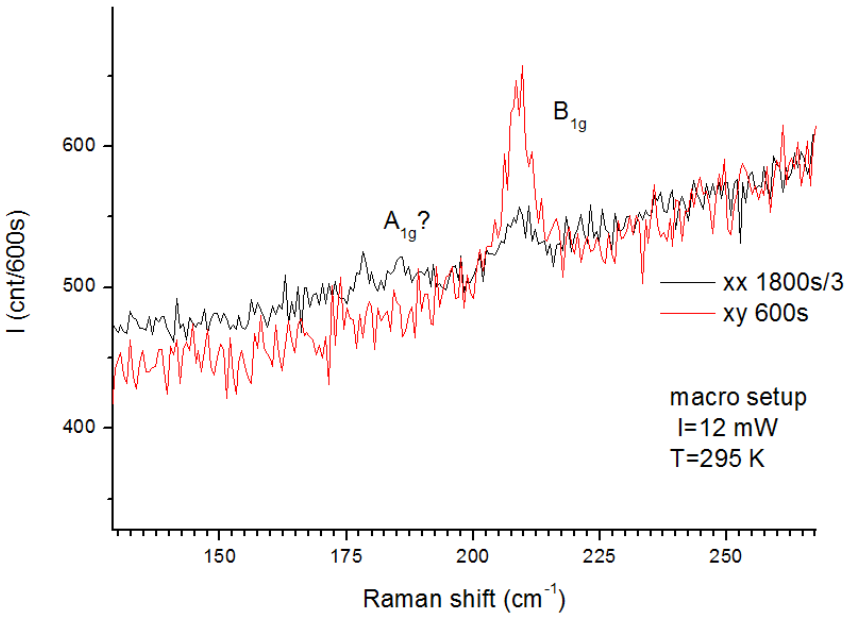

Figure 5-7 First result of the macro setup on the sample at room temperature. The B_{1g}-phonon is clearly visible in the crossed polarization geometry spectrum. In the parallel polarization geometry there is some leakage in polarization components as the B_{1g}-phonon still shows up. The A_{1g}-phonon is still not clearly resolved at room temperature.

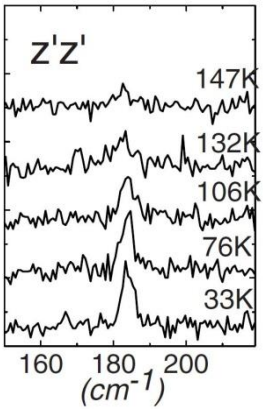

Figure 5-8 Temperature dependence of arsenic A_{1g}-mode by *Chauvière et al.*

The possible answer to the "A_{1g}-phonon problem" was found in an article about the lattice dynamics in $Ba(Fe_{1-x}Co_x)_2As_2$ by *Chauvière et al*.[1] Here a macro setup was used (differences between the micro and macro setup are discussed in paragraph 5.5). A parallel polarization geometry spectrum was made on the parent compound $BaFe_2As_2$ and they "did not observe the arsenic mode A_{1g} (As) at room temperature". The arsenic mode gains considerably in intensity upon cooling as seen in Figure 5-8. The studied sample has some cobalt-atoms substituted for iron-atoms. As cobalt and iron are neighbours in the periodic table, this substitution probably should not give a big difference in lattice vibrations, certainly not vibrations associated with the arsenic atoms. The notification of the absence of the A_{1g} –phonon measured in macro is in agreement with data obtained on our studied sample. This gives an inconsistency in spectra obtained by *Sugai* and *Chauvière* respectively.

So most probable the A_{1g}-phonon will finally show up in the macro setup when the sample is cooled. As the A_{1g}-phonon still didn't show up in the micro measurements at 4K and 30K this will most probably mean that the ratio a/b in the A_{1g} Raman tensor is small.

5.2 Air spectrum.

An unwanted contribution to the Raman spectrum in the low wave number regime is due to the excitation of rotational levels of oxygen and nitrogen. This gives the so-called "air spectrum", observed between 10 cm^{-1} and 190 cm^{-1} at room temperature as shown in Figure 5-9.

[1] (Chauvière, 2009)

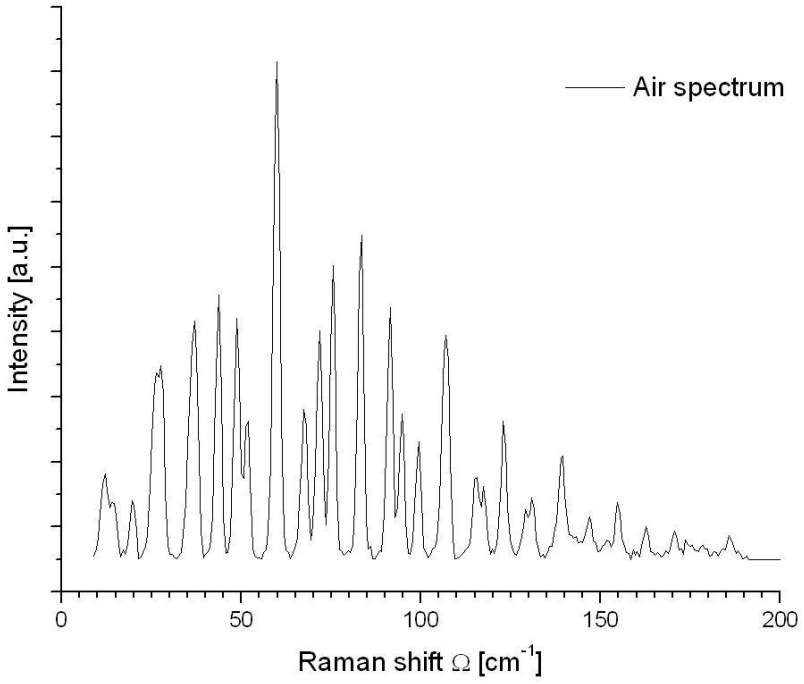

Figure 5-9 Measured air spectrum.

5.2.1 Generation of air spectrum

Oxygen and nitrogen are rotating dumbbells. Elementary quantum mechanics can model oxygen and nitrogen as rigid rotors to explain the form of the air spectrum. The linear rigid rotor model consists of two point masses located at fixed distances from their center of mass. [1,2]

The energy levels of a field-free system are determined by solving the Schrödinger equation $\hat{H}\Psi = \mathrm{E}\,\Psi$ where the Hamilton-operator is given in spherical coordinates. This gives an eigenvalue equation

$$\hat{H}Y_l^m(\theta,\varphi) = \frac{\hbar^2}{2I}\, l(l+1)Y_l^m(\theta,\varphi) \tag{5.2.1}$$

where $\mathrm{Y}_l^m(\theta,\varphi)$ are the spherical harmonics. The eigenvalue

$$E_l = \frac{\hbar^2}{2I}\, l(l+1) \tag{5.2.2}$$

is (2l+1)-fold degenerate. By the introduction of the *rotational constant B*, the energy can be written:

$$E_l = Bl(l+1) \;\text{ with } B \equiv \frac{\hbar^2}{2I} \tag{5.2.3}$$

[1] (en.wikipedia.org/Rigid_rotor)

[2] (rkt.chem.ox.ac.uk/tutorials/rotation/rot_spectra.html)

Here I is the moment of inertia of a rigid rotor, given as $I = \mu R^2$ where μ is the reduced mass of the two atoms. In units of reciprocal length, as used in spectroscopy, the rotational constant is:

$$\bar{B} \equiv \frac{B}{hc} = \frac{h}{8\pi^2 cI} \qquad (5.2.4)$$

If the cgs-system is used for h, c and I, B is given in cm^{-1}. So the rotational constant B depends on the distance between the atoms in a diatomic molecule. The rotational constants for molecular oxygen and molecular nitrogen can be calculated as B_{O_2}= 5,77cm^{-1} and B_{N_2}= 8,00cm^{-1}. The air spectrum consists of a series of peaks that correspond to transitions between energy levels with different l-values. The quantum mechanical selection rules for a rigid rotor are Δm=0 and Δl=±1.

The difference between succeeding energy levels is:

$$\begin{aligned} \Delta E = E_{l+1} - E_l &= Bl(l+1) - B(l+1)(l+2) \\ &= 2B(l+1) \end{aligned} \qquad (5.2.5)$$

This gives an increasing energy difference sequence 2B, 4B, 6B, 8B,… between the rotational levels as seen in Figure 5-10. These transitions show up in the Raman spectrum; rotational peaks appear at energy level differences corresponding to an integer multiple of twice the value of the rotational constant B. As air consists of oxygen and nitrogen, the air spectrum will be composed of two series of rotational peaks, with each their appropriate 2B-spacing between the peaks.

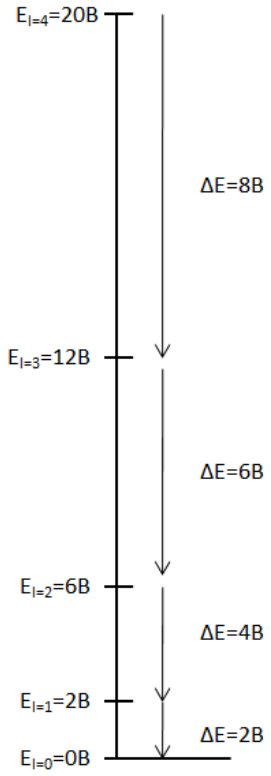

Figure 5-10 Level spacing and energy differences between energy levels for a rotating dumbbell.

The clearly visible modulation originates from the Boltzmann distribution. This distribution gives an interplay between the degeneracy of the energy levels and the factor $\exp\left(-\frac{E_l}{k_B T}\right)$ according to:

$$\frac{N_l}{N} = \frac{(2l+1)e^{-Bl(l+1)/(k_B T)}}{Z(T)} \qquad (5.2.6)$$

where Z(T) is the partition function

$$Z(T) = \sum_l (2l+1)e^{-Bl(l+1)/(k_B T)} \qquad (5.2.7)$$

N is the total number of particles and N_l the number of particles occupying the E_l^{th} energy level, k_B the Boltzmann constant and T the temperature.

As the distance of the two oxygen atoms (or the nitrogen) are not completely fixed, the peaks will be broadened of course to give the experimental air spectrum.

The measured air spectrum was already shown in Figure 5-9. The region between (20-120) cm^{-1} is again shown in Figure 5-11.

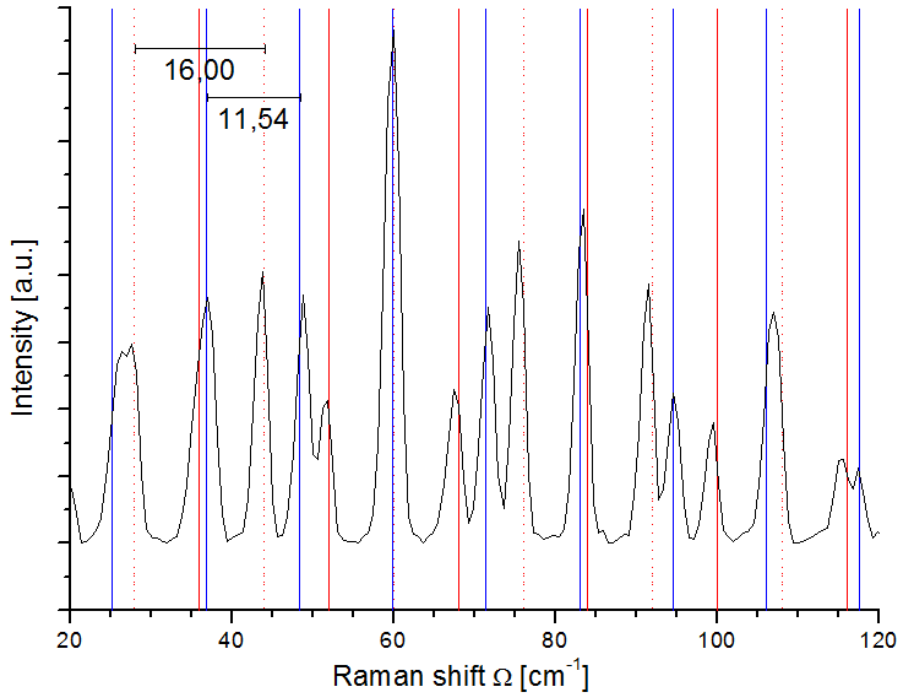

Figure 5-11 Part of air spectrum with 2B spacers. 2B=16,00cm^{-1} (blue for oxygen) and 2B=11,54cm^{-1} (dashed red) for nitrogen. The straight and dashed red lines are all located on peak positions.

The *blue* grid lines are separated $2B_{O_2}$= 11,54cm^{-1} and the *dashed red* lines are separated over distances $2B_{N_2}$= 16,00cm^{-1}. Both grid line sequences show to be in agreement as predicted. The big peak at Ω=60 cm^{-1} is a combination of two unresolved peaks. Apart from these two series of peaks there is also another series of lower intensity peaks (*straight* red lines) separated $1B$= 8,00 cm^{-1} from the high nitrogen peaks (dashed red lines). The origin of this extra series of peaks is not clear.

5.2.2 Problems for determination of electronic scattering

The air spectrum will be a major complication for acquiring good spectra from which one can determine the electronic spectrum. *Outside* the cryostat the height of the biggest peak of the air spectrum is about equally sized to the B_{1g}-phonon when an intensity I=2,5mW is put on the sample. This is measured in optimal configuration for seeing the B_{1g}-phonon mode; the c(xy)c-geometry. As the intensity of the air spectrum is already comparable to the phonon height, the electronic signal surely will be overshadowed by the peaks. So it is of major importance to suppress the generation of the air spectrum.

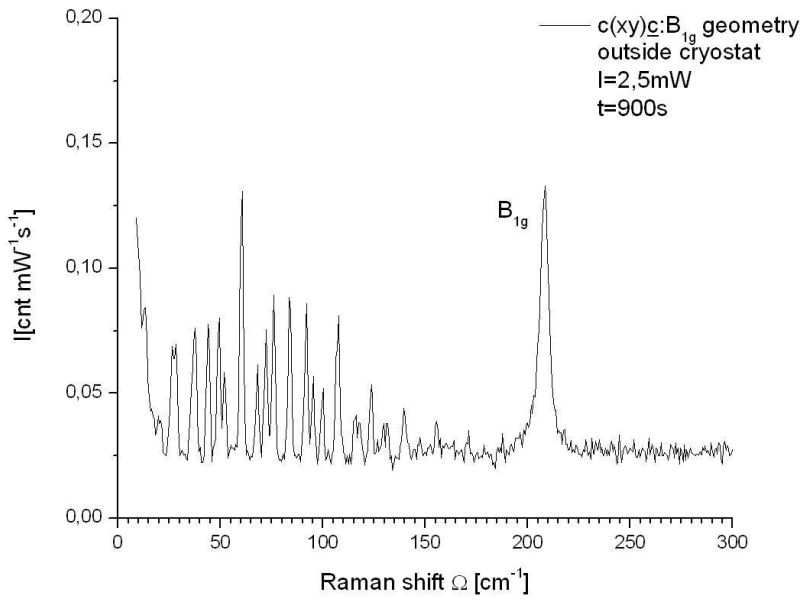

Figure 5-12 The air spectrum poses a serious problem to the determination of electronic excitations in the same wavenumber region. Here the B_{1g} phonon height is compared to the air spectrum.

5.2.3 Tests for reduction of the air spectrum

The air spectrum signal is generated in all focus points in the optics system. As these focus points are nicely imaged on the CCD-chip the air spectrum will show up in measured spectra. Below I will discuss some tests done to see how the air spectrum can be suppressed. The most important focus in the system is of course the focus on the sample. As the sample is placed in a vacuum chamber, the cryostat, this intuitively must give a big reduction in the generation of the air spectrum signal. This suppression factor was determined to be about 0,5. This means that all the focus points outside the cryostat account for about 50% of the total air spectrum.

The practical way to suppress generation of the air spectrum is to flush focus points with an inert gas; argon. Argon does not have rotational levels as it is a monatomic gas. The idea is that argon flows away the oxygen and nitrogen molecules out of the focus point. The focus point before the beam splitter was flushed with argon as this is the most intense focus in the system. This only gave a 5% of reduction of the peaks. Flushing of the pinhole focus by aiming the argon with a needle didn't give a distinguishable difference in the peaks. As the intensity at the last focus point outside the monochromator, located at the entrance slit, is about equal to the intensity at the pinhole, flushing here also doesn't help. The last three focus points are located inside the monochromator. Here the intensity of the light will already be greatly reduced, so these focus points do not make up the 50% of the air spectrum credited to the focus points outside the cryostat. The only conclusion here to be made is that argon flushing of the focus points isn't that effective for reducing the air spectrum as proposed.

A simple solution to the air spectrum problem could be to measure a noise-free air spectrum and subtract this from the spectra measured on the sample, at least if the material is a good scatterer. Of course this is not a preferable solution as this will greatly enhance the error in the resulting electronic signal spectrum. This noise-free air spectrum was measured overnight as an average of

55x15 minutes measurement at I=5mW focused in air. The result of this measurement is found at the beginning of this chapter.

5.3 Rayleigh-wing

The Rayleigh-wing is a phenomenon readily observed when using the micro setup. The name of the phenomenon refers to the elastic scattering of light to particles; Rayleigh scattering. Only one in 100 millions of incoming photons will get a frequency shift to give the Raman spectrum. The other 100 millions of photons are elastically scattered and they also go into the monochromator where this Rayleigh-signal evidently needs to be suppressed not to burn the CCD-chip. Apart from this high intensity at a "Ω=0" shift there will also be diffuse propagation of the light with a small shift to give a big Lorenztian response centered at Ω=0. This diffuse propagation[1] is due to reflection, dirt, surface irregularities, etcetera and temperature dependent as was observed.

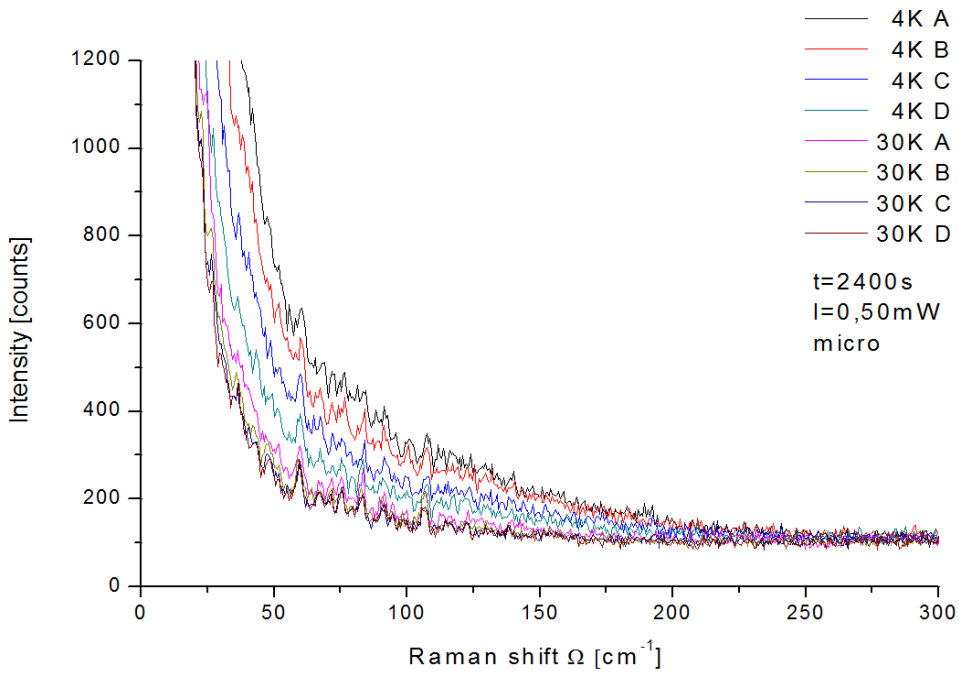

Figure 5-13 The Rayleigh scattering does not remain constant over a measurement day.

The diffuse Rayleigh-scattering signal does not remain constant over a measurement day as can be seen from the above plot. This complicates a reliable determination of electronic scattering as there is no constant background whereupon the electronic signal is superimposed.

The background drift in the 4K may probably be attributed to a slight change in focus in the course of the measurement cycle. Another possibility is that the incoherent scattering increases by the combination of vacuum pumping and cooling at the same time as was done. In this way air particles can still enter the cryostat where they will condense on the sample.

[1] (Kuzmany, 2009), page 214

5.4 Results on probing electronic scattering in micro

Here the most promising results obtained with the micro setup will be discussed. The used geometry is quasi-backscattering. According to literature [1,2] the clearest evidence of a pair breaking signal should be found in c(xx)c-geometry. This polarization geometry gives the $A_{1g} + B_{2g}$ vertex and will probe the electron dynamics of hole bands in the $BaFe_{1.80}Co_{0.20}As_2$ pnictide. The sample was placed in the cryostat and positioned under the right angle with respect to incoming polarization (x-axis of the sample parallel with respect to the optic table, as the incoming polarization is parallel to the short edge of the optic table). The c(xx)c-polarization geometry is then chosen by placing the polarizer horizontal and putting a λ/2-plate for a 90 degree polarization rotation.

4 measurements of 30 minutes at T=4K were made and 4x30minutes of measurements at T= 30K (above T_c) were made with an intensity of (0,50±0,05)mW illuminating the sample to outrule the possibility of heating the sample. The intensity was the same above and below T_c to give a reproducable result. The measurement sequences were averaged and the unedited (apart from despiking) result is given below.

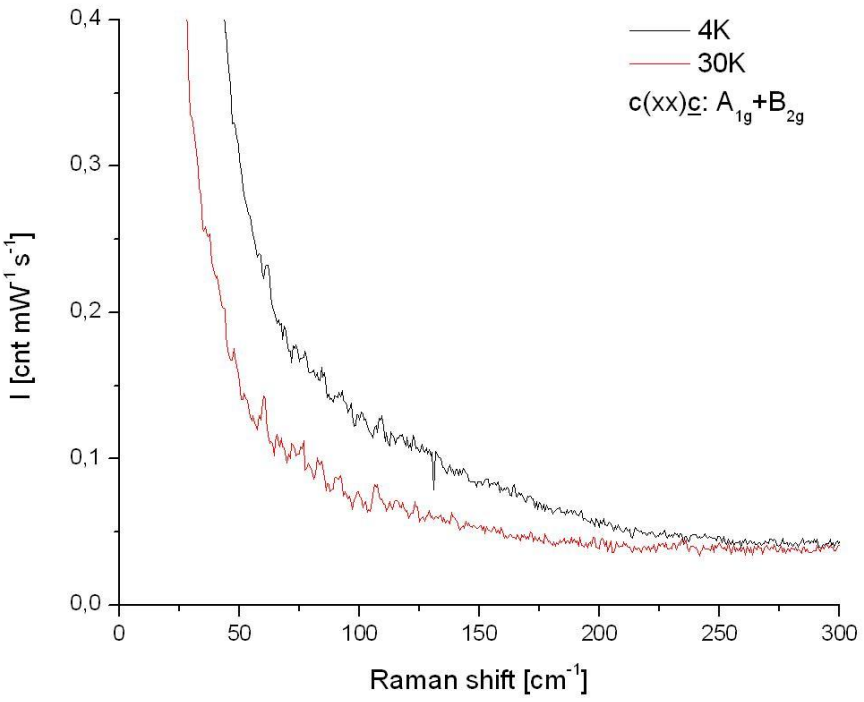

Figure 5-14 The 4K and 30K spectra in the c(xx)c-configuration does not give a clear difference in electronic scattering.

Not that much can be concluded about this plot, except for a change of the Rayleigh-wing intensity. After a background subtraction and scaling for the shifted Rayleigh-wing these spectra were divided by its corresponding Bose-Einstein-factors (n_k+1) and multiplied by the Raman shift according to formula 9.33 from Kuzmany.[3] The (n_k+1) factor assures thermal averaging. Multiplying with Ω

[1] (S.Sugai, 2010)

[2] (Muschler B. , 2009)

[3] (Kuzmany, 2009), chapter 9.2.5

obviously puts the Rayleigh-line in this spectrum at zero intensity, but it merely shows to be a mathematical trick with no physical reason.

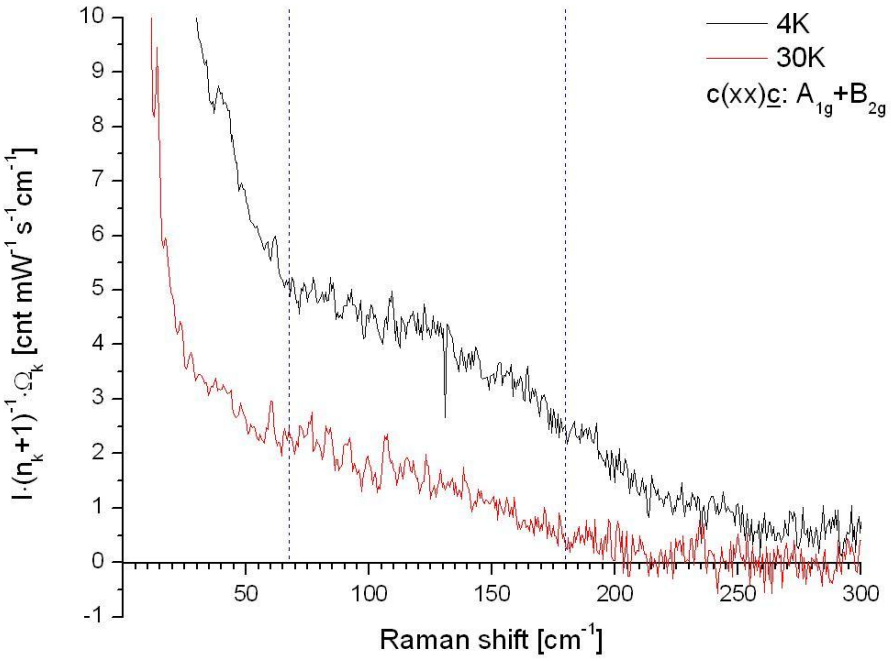

Figure 5-15 After background subtraction, dividing by the Bose-factor and multiplication by the Raman shift the c(xx)c-configuration possibly shows some more scattering in the superconducting state.

Apart from a raise and broadening of the Rayleigh-wing, a change in the slope of the signal in the wave number region from about 67cm^{-1} to 180cm^{-1} can be noticed which can be attributed to opening the superconducting gap. This is of course a result under premise, but this looks like the best result to see evidence of increasing scattering in the SC-state one can get with the micro measurement. Another measurement cycle of 4x40 minutes at 4K respectively 30K was done. This also gives a small alternation in the slope:

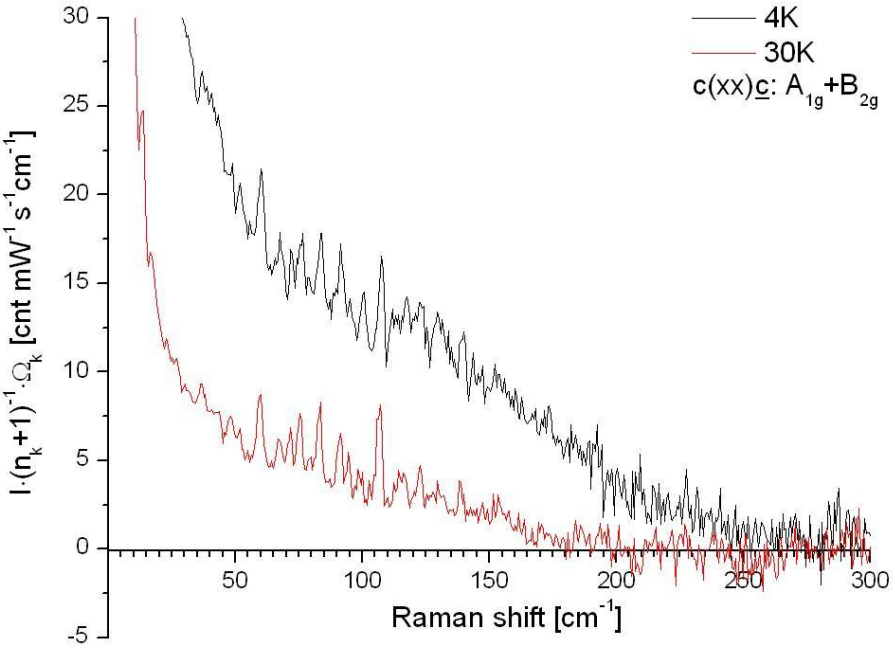

Figure 5-16 40 minutes measurement cycle in c(xx)c-configuration.

5.5 Macro vs. Micro

In this paragraph a comparison between the used micro setup and the macro setup is made regarding experimental differences. Also the differences between both methods for probing electronic dynamics is discussed.

5.5.1 Experimental comparison

General comparison and B_{1g}-phonon count rate

To give a satisfactory silicon count rate the monochromator's entrance slit was widened in the macro setup. This gives a drop in resolution. The resolution was determined by looking at the *half width at half maximum* for the 520 cm^{-1} silicon mode. The *micro* setup has got a resolution of about 1,4 cm^{-1}. The used *macro* setup has got a resolution of about 2,4 cm^{-1}.

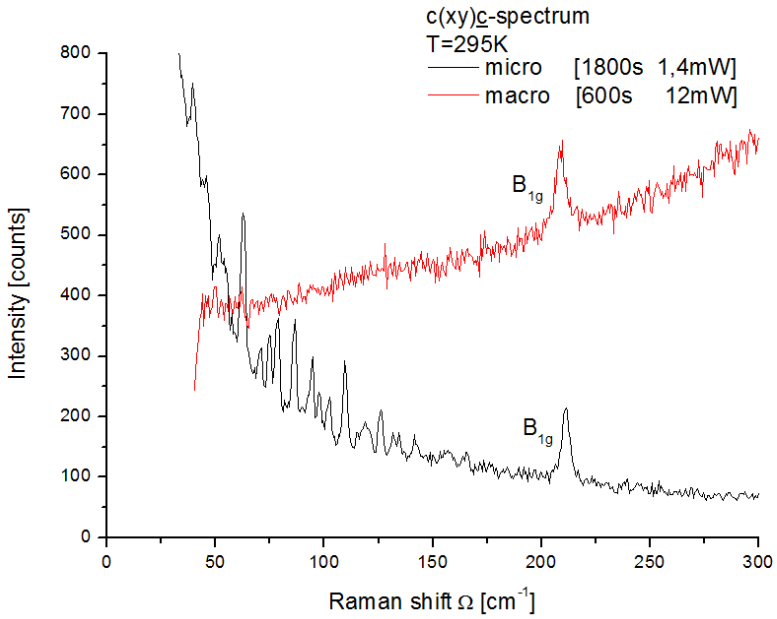

Figure 5-17 Comparison of micro and macro c(xy)c-spectra.

Micro and macro c(xy)c-spectra are shown in Figure 5-15. These are the unedited (expect from despiking) measured spectra taken inside the cryostat. Different integration times and laser intensities were used as given in the figure. An increase in unwanted fluorescence can be seen for the macro setup. This probably originates in the degraded sample quality (it had a crack line, dust) as it was more difficult in our macro setup to illuminate a good quality surface as discussed below.

As the resolution was changed between both methods, the most fair method to compare the count rate for both methods was to integrate the B_{1g}–phonon peak and divide it by integration time and power. The micro setup has 0,28 cnt $mW^{-1}\,s^{-1}$ and the macro setup has 0,15 cnt $mW^{-1}\,s^{-1}$ (full peak integrated) so the count rate remains in the same order of magnitude. This factor 2 loss can possibly be attributed to the non-optimal lens system. The lens system coupled into the monochromator had a too big image on the first mirror of the monochromator.

To compare both used methods one can look at the noise levels. "Signal" is defined as the integral value of the peak. The used "methods" are micro at I=1,4mW and macro at I=12mW. The noise level for the micro measurement is about $N_{micro} \approx \sqrt{100} = 10$. For the macro measurement $N_{micro} \approx \sqrt{500} \approx 23$. This macro noise level will already drop when the background is lowered by reducing the unwanted fluorescence. (total photon count is "wanted" signal + background, noise is square root of total photon count). Integrating the phonon peaks give $S_{micro} \approx 714\ cnt\ cm^{-1}$ and $S_{macro} \approx 1070\ cnt\ cm^{-1}$. As the measurement times vary by a factor 3, the signal-to-noise ratio for macro needs to be multiplied by $\sqrt{3}$. This gives $(S/N)_{micro} \approx 714\ cnt\ cm^{-1}/(10\ cnt) \approx 71 cm^{-1}$ and $(S/N)_{macro} \approx 1070\ cnt\ cm^{-1}/(23 cnt) \approx 46 cm^{-1}$. But as already noticed, the noise level of the macro setup can surely be reduced greatly. The most important remark to be made to these (S/N) values is that the "micro method" is not a good method. The energy density for the micro method is about 30 times higher as the macro method, so the signal level for the micro method needs to be divided by 30 only to give $(S/N)_{micro} \approx 2\ cm^{-1}$. The loss in resolution for the macro setup wasn't considered here.

Sample position

In the micro measurements one has the freedom to rotate the cryostat. In macro the cryostat remains fixed hence the sample needs to be glued in the exact position. The cryostat can be mounted under an angle of 0° and 45° and this 45° angle can possibly give problems with cooling. A limited amount of rotational freedom also gives problems when one wants to measure different scattering configurations.

Air spectrum

The focus points in the micro setup are imaged on the CCD-chip. As there are more focus spots than only the sample focus spot (located inside the cryostat) nicely imaged on the CCD, the air spectrum will show up in micro spectra. The only intense focus in the *macro system* imaged on the CCD is located inside the cryostat (in vacuum) so one does not expect an air spectrum to arise anymore in macro spectra. This idea is confirmed by Figure 5-15.This is a major benefit from the *macro* measurement setup opposed to *micro* where the air spectrum indeed shows up with great intensity as was seen in paragraph 5.2.2.

Rayleigh-wing

In the used *macro setup* configuration the excitation beam will scatter out of the cryostat. The idea is that the greater part of the incoming laser intensity will not enter the monochromator anymore so the Rayleigh-line should be gone (diffuse Rayleigh scattering from the sample and reflection from the cryostat window can enter the monochromator, but this is way less as in the micro setup) . The macro spectrum in Figure 5-15 was only taken up to a Raman shift Ω=50cm^{-1}. The region above 50cm^{-1} shows a suppressesion of the Rayleigh-wing for our trial setup, but still some work needs to be done to ensure that the Rayleigh-wing is gone at lower wavenumbers. As seen in *Muschler et al.* data in Figure 5-18 it should be possible to greatly reduce the Rayleigh-wing in a Raman spectrum when measuring in macro.

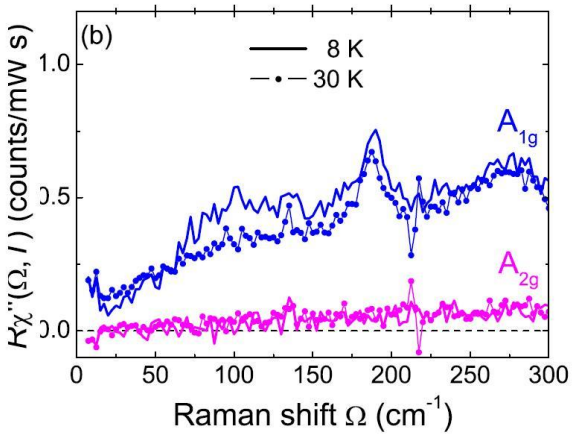

Figure 5-18 In *Muschler et al.* A_{1g} spectrum there is still some laser intensity which is not suppressed, but this is way less as in the micro setup.

Aligning

The alignment process in the *micro* measurements is relatively easy as one has a camera to see the focus spot. This is not the case in the *macro* measurements. As the sample is imaged on the slit with a factor M=4.5 it is still possible to some extent to see where the laser focus is. The focus can be adjusted by the f=15cm lens but this is still guesswork in the setup as it was installed.

Energy density

A big drawback for the *micro* measurement is that the acquired amount of signal is bound to the use of a safe energy density. When the impinging laser power is too high the sample will heat up. This is obviously unwanted when studying superconductors. The name *micro* comes from the small laser spot size on the sample. This spot size is about $9\mu m^2$ for the micro setup. A safe guess for the macro spot size is about $50x50\mu m^2$. This bigger spot size allows for the use of more power hence more electronic scattering.

Sample quality

When measuring in micro it is easy to find good spots on a sample. The macro measurement needs a good quality sample with as less as possible dirt as one will illuminate almost the complete sample. Dirt, irregularities, etcetera will give rise to unwanted fluorescence.

5.5.2 Macro vs. micro for probing electronic scattering

The benefit from *macro* especially for probing electronic scattering is that one will get a Raman signal almost solely from the material itself. No air spectrum is generated and not that much Rayleigh-wing-scattering will show up. In this way one is not bound to subtraction of an air spectrum and a Lorentz function to get the electronic scattering.

For determination of gap symmetries macro also looks the only correct option. For instance, A_{1g} channels do not give rise to a flat electronic continuum in the normal state as can be seen in Figure 5-18 so dividing superconducting electronic spectra by the normal state spectra can be quite tricky.

6 Conclusions

Determination of superconducting gap symmetries in $Ba(Fe_{1-x}Co_x)_2As_2$ showed to be a nontrivial task, both the theoretical treatise and the experimental part.

An overview of the theoretical treatise of electronic Raman scattering on superconductors was given in chapter 2 and 3. Raman spectroscopy is a momentum dependent technique which allows for probing different parts of the Brillouin Zone simply by choosing the appropriate polarization geometries. This is because of the Raman vertex which is proportional to electronic charge fluctuations in momentum space. The Raman vertex on itself is again coupled to different polarization geometries and irreducible representations of the space group to which a studied material belongs. The superconducting signal is described by the so-called Tsuneto-Maki function.

Experimental determination of gap symmetries with a *micro setup* showed to be the wrong way. A micro setup generates a clearly visible air spectrum and incoherent Rayleigh-wing scattering. These two effects arise in the low wave number regime where one wants to probe the electronic excitation. Furthermore one is bound to use a safe energy density on the sample. After these notifications it was realized that only a *macro setup* is appropriate to acquire solely the electronic scattering signal. A first macro spectrum showed the absence of the air spectrum.

By a background subtraction, division by the Bose-factor and multiplication by the Raman shift Ω a possible increase in electronic scattering arising from breaking of Cooper pairs on the hole bands in the wave number region from about $67cm^{-1}$ to $180cm^{-1}$ was noticed in the micro measurements.

Considerable attention was paid to the A_{1g} phonon as it did not show up in the micro measurements at 295K respectively 4K. The macro measurement at T=295K also didn't show the A_{1g} phonon in disagreement with *Sugai et al. Chauvière et al* made an explicit notification of the absence of the A_{1g} phonon mode at room temperature in $BaFe_2As_2$. This possibly means that the A_{1g} phonon shows up in our measurements at lower temperatures.

7 Recommendations for future work

The installed macro setup was just a quick “trial version” to probe the phonons in the $Ba(Fe_{1-x}Co_x)_2As_2$ sample. Of course the used macro setup is still not satisfactory enough from making excellent measurements of electronic scattering. Evident improvements can already be made by using dichroic mirrors instead of the simple mirrors used in our trial setup. Also more signal can simply be gained by optimizing the lens system coupled into the monochromator. In the used setup the image on the first mirror of the monochromator covered an area about twice as big as the first mirror. This is already a big loss of signal.

Also attention needs to be paid to the angle of the incoming laser. In the trial setup the reflected laser line clipped the cryostat window frame. This gives unwanted diffuse scattering. The incoming laser beam also needs to be chosen according to the Brewster-angle. Here the transmission of light with polarization vector in the plane of incidence is maximal.

One evident improvement regarding sample is to treat it more carefully. Dust, scratches and cracks will greatly reduce the quality of spectra by increased diffuse scattering and fluorescence. The sample should at least have a perfect quality part of about $50x50\mu m^2$, but this should of course be possible as samples of a size of $2x2mm^2$ surely could be grown.

The method of angular dependence of a phonon for determination of the sample’s crystal axes has an uncertainty of about 5° as can be seen in Figure 5-2. Taking a Laue image of the sample to determine the crystal axes could reduce the uncertainty.

The last macro problem regarding the sample is that there was no possibility of rotating the cryostat apart from a 45° angle. A possible solution to this problem could be to craft circular copper plates whereupon the sample can be glued. This copper plate needs to be drilled with sets of 2x4 holes which are 45° apart. In this way one can easily switch between the xx/xy-system and the aa/ab-system. Another idea is to drill channels in the copper plate. These ideas are drawn Figure 7-1.

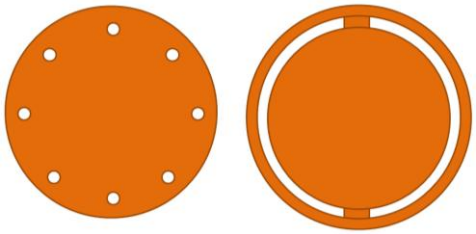

Figure 7-1 Just two ideas of copper plates which allow for angular variation.

8 Acknowledgements

This bachelor project posed some serious difficulties along the way which were not anticipated beforehand. Some days I seriously asked myself why I was so stubborn not to listen to Toni's advice not to choose this topic as I would "get a hard time". But the reason to ignore this advice was that the topic *superconductors* speaks to ones imagination. In the end the result was more a "how to determine" than a finite result on what the gap symmetries in the studied material were. Of course this is somewhat of a disappointment, but finally finding the clue of how to determine electronic excitations in an appropriate way was maybe even more satisfactory.

First of all I would like to thank Toni for his experimental guidance. I think I learned quite a big deal about the Raman setup, Raman spectroscopy, cryo technique and of course other things not directly relevant to this research project.

Of course I would also like to thank Prof. Dr. Ir. Paul van Loosdrecht for his guidance and coming up with this topic. At the start of the 3rd year I took his *Photons and Matter* course and I'm very glad I did so. This actually gave the first look to Condensed Matter Physics in the complete bachelor curriculum. Hopefully I can occupy myself in this physics area quite a few more years.

I would also like to thank Dr. Matteo Montagnese. We had some interesting discussions about the theoretical parts as the Brillouin Zone harmonics and what the Final-State interaction actually was. Also I will never forget his discussions on for instance "what is the best Italian restaurant in Groningen", "why do people always start with the good news" and "why do I prefer the Italian educational system above the Dutch system".

Of course I must not forget to thank the technicians Ben Hesp and Foppe de Haan.

And last but not least I would also like to thank all other OCMP group members and students in the group for having a really nice time!

Rolf

9 Bibliography

Articles

1. T.P. Devereaux, R. Hackl, Inelastic light scattering from correlated electrons, Reviews of Modern Physics **79**, 175 0034-6861/2007/79(1)/175(59) (2007)
2. G.R. Boyd, P.J. Hirschfeld, T.P. Devereaux, Effect of disorder on the electronic raman scattering in the superconducting state of iron pnictides, Phys. Rev. B. **82**, 134506 (2010)
3. G.R. Boyd, T.P. Devereaux, P.J. Hirschfeld, V. Mishra, D.J. Scalapino, Probing the pairing symmetry of the iron pnictides with electronic Raman scattering, Phys. Rev. B. **79**, 174521 (2009)
4. S. Sugai, Y. Mizuno, K. Kiho, M. Nakajima, C.H. Lee, A. Iyo, H. Eisaki, S. Uchida, Pairing symmetry of the multiorbital pnictide superconductor $BaFe_{1.84}Co_{0.16}As_2$ from Raman scattering, Phys. Rev. B. **82**, 140504(R) (2010)
5. B. Muschler, W. Prestel, R. Hackl, T.P. Devereaux, J.G. Analytis, Jiun-Haw Chu, I.R. Fischer, Band and momentum-dependent electron dynamics in superconducting $Ba(Fe_{1-x}\ Co_x)_2As_2$ as seen via electronic Raman scattering, Phys. Rev. B. **80**, 180510(R) (2009)
6. D.C. Johnston, The puzzle of high temperature superconductivity in layered iron pnictides as chalcogenides, Advances in Physics,**59** 803-1061 (2010)
7. H. Monien, A. Zawadowski, Theory of Raman scattering with final-state interaction in high-T_c BCS superconductors: Collective modes, Phys. Rev. B. **41**,8798 (1990)
8. L. Chauvière, Y. Gallais, M. Cazayous, A. Sacuto, M.A. Méasson, Doping dependence of the lattice dynamics in $Ba(Fe_{1-x}\ Co_x)_2As_2$ studied by Raman spectroscopy, Phys. Rev. B. **80**, 094504 (2009)
9. J. Paglione, R.L. Greene, High-temperature superconductivity in iron-based materials, Nature Physics **Vol 6**, 645-658 (2010)

Theses

1. B. Muschler, Walther-Meissner-Institut, Von einer Fermi-Flüssigkeit zu einem dotierten Antiferromagneten:Eine Raman-Studie (2007)
2. D. Fausti, University of Groningen, ZIAM-OCMP, Phase Transitions and Optically Induced Phenomena in Cooperative Systems (2008)

Websites

1. Bilbao Crystallographic Server, retrieved from http://www.cryst.ehu.es./rep/sam.html
2. Article on Rigid Rotor, retrieved fromhttp://en.wikipedia.org/wiki/Rigid_rotor
3. Site on rotational spectra, retrieved from http://rkt.chem.ox.ac.uk/tutorials/rotation/rot_spectra.html

Literature

1. M.J. Lax, Symmetry Principles in Solid State and Molecular Physics
2. C. Kittel, Introduction to Solid State Physics, 8^{th} ed. (2005)
3. H. Kuzmany, Solid State Spectroscopy, 2^{nd} ed. (2009)